Modeling and Simulation of Trapping Mechanisms of Granular Media in Space *

Marco B. Quadrelli †, Paolo Ius‡, Luca Lanzoni§

This paper describes the modeling and simulation of trapped granular media, within the context of the Granular Imager project. We describe the physics of trapped granular media in space, and the methodologies used to stably confine and shape such a medium using electromagnetic fields. The numerical models have also been validated with results in the literature, obtaining excellent agreement. The results of the numerical tests indicate that it is possible, with structural arrangements of rings and plates at different levels of electrostatic potential, to stably confine one or more charged particles, when driven by voltages that can be modulated in time and space.

Contents

I Introduction **1**

II Mechanisms for Particle Trapping and Confinement **2**
- A Paul Trap . . . 5
- B Penning Trap . . . 8

III System Configuration **10**

IV Equations of Motion of Orbiting Granular Systems with Contact **13**

V Numerical experiments **16**
- A Model Validation . . . 16
- B Experiments with rings and plates . . . 18
  - 1 Configuration with two electrodes: one ring and one plate . . . 18
  - 2 Configuration with two electrodes: two rings . . . 18
  - 3 Configuration with three electrodes: one ring, two plates (first parameter set) . . . 19
  - 4 Configuration with three electrodes: one ring, two plates (second parameter set) . . . 19
- C Example of cloud containment by equivalent fans . . . 22
- D Magnetic Levitation Model . . . 23
- E Inverse determination of electric and magnetic fields for cloud re-shaping . . . 23

VI Conclusions **25**

I. Introduction

Orbiting Rainbows is a Phase II NASA Innovative Advanced Concepts (NIAC) study that is looking twenty years into the future of creating a space-based observatory from granular media. Recent accomplishments of this project are documented elsewhere,[15],[16].[17]

*©2016. All rights reserved.

†marco.b.quadrelli@jpl.nasa.gov, Mobility and Robotic Systems Section, Autonomous Systems Division, Jet Propulsion Laboratory, California Institute of Technology, 4800 Oak Grove Drive, Pasadena, CA 91109

‡graduate student, Politecnico di Torino, Italy

§graduate student, Politecnico di Milano, Italy

The goal of this research is to identify ways to optically manipulate and maintain the shape of a cloud of dust-like matter so that it can function as an adaptive surface with useful electromagnetic characteristics in the optical or microwave bands. We call this concept the *Granular Imager*. The investigators are performing fundamental research and developing the technology roadmap to construct an optical system in space using nonlinear optical properties of a cloud of micron-sized particles, shaped into a specific surface by light pressure, to form a very large and lightweight aperture of an optical system. This cloud optic will be relatively simple to package, transport, and deploy. It is reconfigurable and can be re-targeted; the focal length is variable and it will be self-healing and ultimately disposable. With near-term plans to build 30 meter ground-based telescopes for astronomy, the demand for higher resolution optics in space continues to grow not only for exo-planet detection, but also for earth-based science, including hyper-spectral imaging and for monitoring of the oceans and land masses (e.g. seismic monitoring).

The Orbiting Rainbows paradigm is unique because of: a) The avoidance of any physical structure and sensing/actuation hardware on the primary, so sensing and actuation are done "at-a-distance" on an amorphous cloud, and all operational complexity is done outside the primary. b) The reliance on optical trapping and manipulation to enable that action "at-a-distance" (although, other mechanisms such as electrodynamic trapping and confinement are also being investigated), and c) The relaxation of the requirements on the fine cloud control by doing the best possible job in software via robust computational imaging algorithms. A typical orbital scenario would follow these steps: (1) the cloud is first released; 2) it is electromagnetically trapped to avoid dissipation and disruption by gravitational forces and shaped into a two-dimensional object (coarse figure control); and 3) the grains could be aligned to the incoming wavefront by means of rastering laser beams (fine figure control) leading to a surface with acceptable imaging characteristics, i.e. the primary aperture. By modulating the spatial and temporal distribution of the confining fields, the cloud can be retargeted as desired. The secondary would be in formation flight with the primary aperture.

The aim of this research was to investigate the modeling and simulation of trapped granular media by considering a few concepts of electrodynamic trap that could be capable to confine and shape a cloud made of charged particles. Each possible design was then tested in order to compare the desirable behavior to the obtained results. Using specific parameters it was possible to define interesting particle arrangements that could be useful for the main mission purposes. We focused our attention on two different configurations that provided us three different remarkable results. One of those two designs in fact could obtain two different cloud patterns depending on the values and parameters we set. The first contribution of this thesis was finding two main concepts, which could be useful for the mission purpose. One of them used two plates electrodes and a ring electrode, the second used two rings. The latter had the capability not to obstruct the light path, and the first, using specific parameters, could arrange the particles in an annulus shape as the mission concept required. The second important contribution of this research was providing a new mathematical model that has more degrees of freedom and that is more complete than the mathematical model frequently used for describing the behavior of ion traps (based on Mathieu equations). This mathematical model in fact provided the same results obtained by Mathieu model just as a specific case. We have considered multiple charge particles, with different charge to mass ratios, and studied their response when confined by a mechanism of ion trapping. The system geometries that have been considered include a system of concentric charged rings, and a system with rings and electrode plates so that a spatial distribution of electric field can be generated and modulated. Both two-dimensional and three-dimensional configurations have been analyzed numerically by propagating the equations of motion of the charged particles in the time domain. The numerical model has also been validated with results in the literature, obtaining excellent agreement. The results of the numerical tests indicate that it is possible, with these structural arrangements of rings and plates, to stably confine one or more charged particles, when driven by voltages that can be modulated in time and space.

The paper is organized as follows. Section II describes the state-of-the-art in mechanisms for particle trapping and confinement. Section III describes the system configuration of the Granular Imager. Section IV summarizes the development of the equations of motion of this system, using the Chrono::Engine formalism. Section V describes the results of several numerical experiments, and Section VI concludes the paper.

II. Mechanisms for Particle Trapping and Confinement

We have been exploring options for trapping and confinement based on techniques being used to contain and levitate atmospheric aerosols (clouds of ice crystals) in ground laboratories. Some of these include

aerodynamic levitation, acoustic levitation, optical levitation, electric levitation, magnetic levitation, radio-frequency levitation and superconducting levitation. The most promising techniques are based on electrodynamic trapping using electrodynamic balances. There are different possibilities that are relevant to the Orbiting Rainbows task (i.e., levitation in vacuum). Some of these options are shown in Figure 1. These are:

- Electrodynamics levitation: Small particles can be confined by electrodes in an electrostatic trap (Penning trap). A Paul trap includes a lateral magnetic confinement field, which adds stability. A major issue in levitation is particle stability, and stability requires that the suspended object have forces exerted on it, which return it to its initial position when it is slightly displaced from that position.
- Parallel plate capacitor. Since the parallel plate Millikan condenser cannot exert a restoring force on a charged droplet in either vertical or horizontal directions, the particle drifts.
- Electrostatic balances. Although the electrostatic balance of Millikan does not provide stable suspension, the use of electro-optic feedback control allows for a weak restoring force in virtue of the electrode shape.
- Electrodynamic balances. By inserting a ring electrode at the center plane between the plates of a Millikan condenser and by applying an AC potential to the ring electrode, the charged particle can be focused at the center of the balance.
- Lorentz coupling with the planetary magnetic field, assuming that the grain is electrically charged.
- Optical levitation. In a three-dimensional gradient-force optical trap for microscopic dielectric particles was demonstrated in 1986. They showed that low-absorbing, dielectric spherical particles with an index of refraction higher than that of a surrounding liquid could be trapped in three dimensions by use of a strongly focused Gaussian laser beam. This phenomenon was suggested earlier for moving atoms and more recently has led to biomedical and related applications involving micromanipulation of living cells, chromosomes, and motor proteins. However, the conventional gradient-force trap based on the design of Ashkin has some limitations. Trapped particles are susceptible to optical damage by absorptive heating because the center of the trap is located in the high-intensity focal region of the beam. Another limitation is that multiple particles may be attracted into the same trap; thus isolating a single particle requires dilute samples. Furthermore, the trapping of low-index particles such as bubbles and droplets or of absorbing particles such as metallic fragments requires a rotating beam when a conventional gradient-force trap is used. There are probably other options, involving multi-physics coupling at different levels.

Two or more atoms stripped of their outer electrons, trapped by electric fields array themselves in structures that behave like both liquids and solids. The possibility of achieving a regular structure of a plasma and the ability of this plasma to be controlled remotely by the direct control of electric and magnetic fields lead us to the concrete realization of an adaptive and re-configurable lens.

Employing the control over the temperature and position of ions (atoms stripped of one or more of their electrons) it is possible to obtain a particular state of matter called microplasma by extension from the large groups of ions and electrons known as plasmas. A microplasma is made by applying electric fields in order to confine a certain amount of ions in a specified region of space. Consequently a cooling process called laser cooling cools the ions near to zero kelvin. The final temperature is related to the behavior of the ions as a whole entity. As it is explained below, the lower is the temperature, the more solid-like the behavior of the plasma will be. Microplasmas can serve as models for the dense plasmas in stellar objects. Like the atoms in liquids, the ions in some cold microplasmas can diffuse through a somewhat ordered state. In other cases, the ions can resemble the atoms in solids, diffusing very slowly through a crystal lattice. The nature of microplasmas is quite different from that of conventional liquids and solids. Whereas common liquids and solids have densities of about 10^{23} atoms per cubic centimeter, microplasmas have concentrations of about 10^8 ions per cubic centimeter. Furthermore, whereas internal attractive forces between the atoms hold conventional liquids or solids together, external electric fields hold the trapped ion microplasmas together. Indeed, the ions, which all have the same charge, actually repel each other and tend to disperse the microplasma.

The specific heat, melting point and other thermodynamic properties of a *one-component* plasma depend greatly on the density and the temperature of the mobile particles; This explains why the electromagnetic

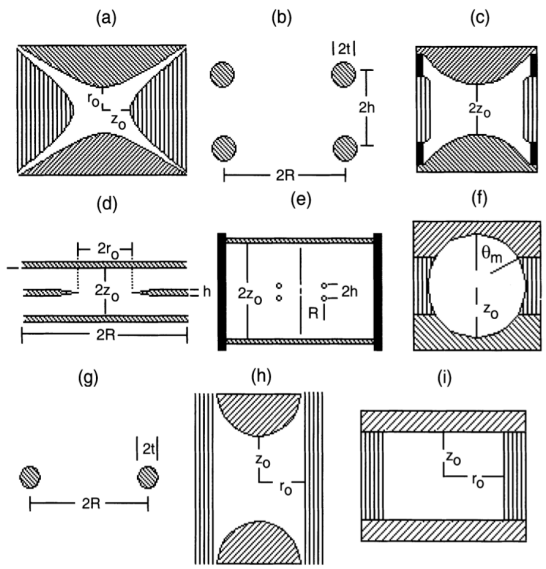

Figure 1. Various types of electrodynamics traps, from[2]

confinement is essential in order to obtain and manipulate the physical properties of a one-component plasma. The dimensionless parameter which express the structural behavior of the plasma is called the coupling. It can be derived from the temperature and the particle density, and it provides a measure of how strongly the neighboring ions interact. The coupling is defined as the Coulomb potential energy between nearest neighboring ions divided by the kinetic energy of the ions:

$$Coupling = \frac{V_{C_i}}{E_{K_i}} \tag{1}$$

The Coulomb potential energy V_C depends on both the average distance between the ions (a function of density) and the charge of the ion species

$$V_{C_{ij}} = \frac{1}{4\pi\epsilon_0}\frac{q_i q_j}{|r_{ij}|} \tag{2}$$

in which q_i and q_j are multiple of the elementary charge (the smallest conventional charge) $e = 1.602 \times 10^{-19}C$. The kinetic energy E_K is simply the temperature (T) multiplied by a physical constant known as the Boltzmann constant $K_B = 1.3806 \times 10^{-23} m^2 kg\, s^{-2} K^{-1}$

$$E_K = T\, K_B \tag{3}$$

Hence the value of the coupling parameter describes the global behavior of this particular plasma (Tab.1). When the Coulomb potential energy is less than the kinetic energy ($Coupling < 1$) the one-component plasma should have no obvious structure and should behave like a gas. But a one-component plasma whose coupling is greater than one ($Coupling > 1$) should show some spatial order. In such strongly coupled one-component plasmas, the ions should stay away from each other because the repulsive Coulomb forces are greater than the thermal forces. At couplings of two or more, a plasma should exhibit liquid behavior. At $Coupling \simeq 180$, a one-component plasma should change from a liquid to a solid phase, in which the ions are arranged in a body-centered cubic crystal.

The predictions are valid as long as the ions in the plasma behave classically and the number of ions is sufficiently high (for one-component plasmas the theory pertain "infinite" systems), that is, as long as the effects of quantum mechanics can be neglected. Under conditions of high density and low temperature, quantum mechanics can be important.

Let us consider a one-component plasma made of dissipative particles in a controlled outer space environment. These particles behave like ions once they are hit by space radiations. The hypothesis are:

Coupling value	Physical characteristics
$C < 1$	*Gas*
$C > 1$	*Gas-Liquid transition*
$C > 2$	*Liquid*
$C > 180$	*Solid lattice*

Table 1. Different behaviors of one-component plasma depending on the coupling value.

$T_{eq} = 300K$, $Q = 10^{-14}C$, hence we obtain

$$E_K = T\,K_B = 4.14 \times 10^{-21} J \tag{4}$$

$$V_{C_{ij}} = \frac{1}{4\pi\epsilon_0}\frac{q_i q_j}{|r_{ij}|} = \frac{1}{r} 8.9877 \times 10^{-19} J \tag{5}$$

$$Coupling = \frac{V_{C_i}}{E_{K_i}} = \frac{1}{r} 2.1709 \times 10^2 \tag{6}$$

which r could be considered an evaluation variable in order to obtain all the possible plasma structures.

Coupling value	Value of r	Physical characteristics
$C < 1$	$r > 2.1709 \times 10^2 m$	*Gas*
$C > 1$	$r < 2.1709 \times 10^2 m$	*Gas-Liquid transition*
$C > 2$	$r < 1.0854 \times 10^2 m$	*Liquid*
$C > 180$	$r < 1.2061 m$	*Solid lattice*

Table 2. Values of the distance within the ions in order to obtain the given structural behavior.

Hence we can achieve a different global behavior simply by varying the average distance that separates ions (Tab.2). One method is the electrode active-control that acts on the V_C parameter by varying the electromagnetic field intensity, otherwise the other parameter we can change is the temperature (E_K) by heating or cooling the one-component plasma.

Because the thermodynamic properties of a one-component plasma depend only on the coupling, a one-component plasma that is cool and diffuse can have the same properties as a one-component plasma that is hot and dense.

The configuration of the Paul trap and the Penning trap are the same; they both consist of a cylindrical symmetrical structure composed by three electrodes. one is *ring* electrode and the other two are *end-cap* electrodes. The difference between the two type of trap regards the nature of the inside fields.

In the Paul trap there is a combination of DC and radio-frequency voltages applied to the electrodes. The equations of motion of an ion inside the this type of trap are Mathieu differential equations,[24] which lead to both stable and unstable solutions depending on the operating parameters. By controlling these parameter, ions of a desired m/e range can be confined, other ions which are intrinsically unstable or have large amplitudes collide with the trap or are lost. All the traps here described are used to confine any charged particle, so we refer to these charges calling them ions.

The Penning trap uses an axial magnetic field and in addition an electric field with both the end-cap electrodes at positive potential (for positive ions/charges) with respect to the ring electrode. The associated radial electric field is repulsive and tends to push ions out of the trap. It is the axial magnetic field which forces the ions into stable epicyclic trajectories resulting in their confinement.

A. Paul Trap

We will now provide a conceptual explanation of how and why the Paul trap works.

In order to understand the operation of Paul trap we firstly start considering the ion motion in a two-dimensional quadrupole device and then extend the concept to a three-dimensional quadrupole field which is the basic form of Paul trap concept. It is also useful to consider firstly the form of the electromagnetic

potential of the quadrupole field and then move to the single ion motion in the two-dimensional and three-dimensional field.

In three-dimensional space the quadrupole field potential is given by

$$\phi = \frac{\phi_0}{2r_0^2}(\lambda x^2 + \sigma y^2 + \gamma z^2) \tag{7}$$

where ϕ_0 is an externally applied electric potential, λ, σ, γ are constants that depend on the nature of the field, and r_0^2 depends on the physical structure of the field. To satisfy the Laplace equation we write

$$\nabla^2\phi = \frac{\phi_0}{2r_0^2}(2\lambda + 2\sigma + 2\gamma) = 0 \tag{8}$$

so this is verified if

$$(\lambda + \sigma + \gamma) = 0 \tag{9}$$

in the trivial case of $\phi_0 = 0$.

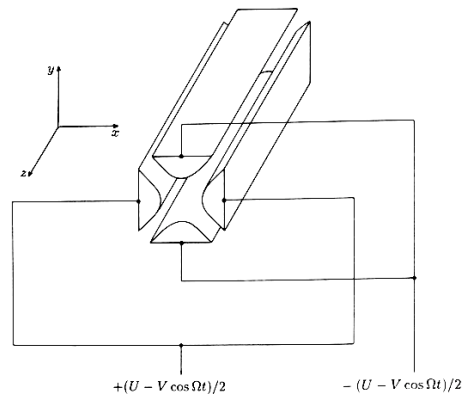

Figure 2. Electrode structure of a two-dimensional quadrupole field

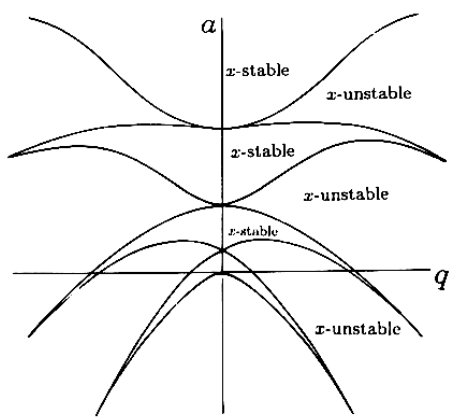

Figure 3. Stability diagram for Mathieu equations.

In the two-dimensional quadrupole field (Fig.2) the coordinate $z = 0$. In the specific case in which $\lambda = -\sigma = 1$ the potential equation is a function of x and y assumes the following form:

$$\phi(x, y) = \phi_0 \frac{(x^2 - y^2)}{r_0^2} \tag{10}$$

This is possible if the potentials on the surfaces of the four rods that constitute the device are $\pm\phi_0/2$ in which $\phi_0/2 = (U - V\cos\Omega t)/2$ and U is the DC voltage and $V\cos\Omega t$ is the radio-frequency voltage of angular velocity Ω.

$$\phi(x, y, t) = (U - V\cos\Omega t)\frac{(x^2 - y^2)}{2r_0^2} \tag{11}$$

The result is that the equations of motion of a charged particle characterized by a given m/e are

$$\ddot{x} + \frac{e}{mr_0^2}(U - V\cos\Omega t)x = 0 \tag{12}$$

$$\ddot{y} + \frac{e}{mr_0^2}(U - V\cos\Omega t)y = 0 \tag{13}$$

$$\ddot{z} = 0 \tag{14}$$

In this case the particle will move along z-axis with constant velocity due to 2D simplifications. Introducing the following substitutions

$$\frac{4Ue}{mr_0^2\Omega^2} = a \tag{15}$$

$$\frac{2Ve}{mr_0^2\Omega^2} = q \tag{16}$$

$$\Omega t = 2\zeta \tag{17}$$

the equations along x-axis and y-axis become

$$\frac{d^2x}{d\zeta^2} + (a - 2q\cos 2\zeta)x = 0 \tag{18}$$

$$\frac{d^2y}{d\zeta^2} - (a - 2q\cos 2\zeta)y = 0 \tag{19}$$

that are the so called Mathieu differential equations for x and y.

Depending on the parameters a and q the Mathieu equation has *stable* or *unstable* solutions. The symmetry properties along a-axis (Fig.3) means that if a stable solution is found for a couple of a, q then the same stable solution must be found for the couple $a, -q$. In order to achieve a stable motion of the ion both solutions of the two Mathieu equations must be stable, so if we compute the results we can define the stability values for the parameters a and q, and then x and y. In three-dimensional space the quadrupole field potential is given by

$$\phi = \frac{\phi_0}{2r_0^2}(\lambda x^2 + \sigma y^2 + \gamma z^2) \tag{20}$$

We assign the values to the three constants as $\lambda = 1$, $\sigma = 1$, $\gamma = -2$, in this case the geometry of the structure allows us to write $r_0^2 = 2z_0^2$. Hence the potential has the form

$$\phi = \phi_0(\frac{x^2 + y^2 - 2z^2}{2r_0^2}) \tag{21}$$

and leads to the following equation of motion:

$$\frac{d^2r}{dt^2} + \frac{e}{mr_0^2}(U - V\cos\Omega t)r = 0 \tag{22}$$

$$\frac{d^2z}{dt^2} + \frac{e}{mr_0^2}(U - V\cos\Omega t)z = 0 \tag{23}$$

Introducing the following substitutions

$$\frac{8Ue}{mr_0^2\Omega^2} = a_z = -2a_r \tag{24}$$

$$\frac{4Ve}{mr_0^2\Omega^2} = q_z = -2q_r \tag{25}$$

$$\Omega t = 2\zeta \tag{26}$$

the Mathieu equations 22 and 23 become

$$\frac{d^2r}{d\zeta^2} + (a_r - 2q_r\cos(2\zeta))r(\zeta) = 0 \tag{27}$$

$$\frac{d^2z}{d\zeta^2} - (a_z - 2q_z\cos(2\zeta))z(\zeta) = 0 \tag{28}$$

Some typical Paul trap trajectories are given in the figure 4. One can notice an high-frequency micro-motion and a secular low-frequency motion.

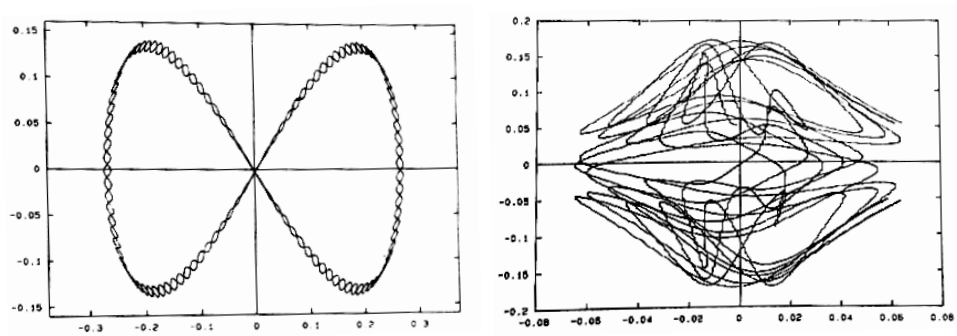

Figure 4. (left) Trajectory of a charged positive ion in a Paul trap. $a_z = -3.5 \times 10^{-6}$, $q_z = 0.095$ **in** $x - z$ **plane. (right) Trajectory of a charged positive ion in a Paul trap.** $a_z = -0.6$, $q_z = 1.2$ **in** $x - z$ **plane. (Pradip K. Ghosh, Ion Traps, Clarendon Press, Oxford 1995, p.17).**

B. Penning Trap

The structure of this trap is identical to the previous one: three electrodes, two end-caps and one ring electrode. What that makes this trap different from the Paul trap is that this doesn't use the radio-frequency field, but it uses a uniform magnetic field along z-axis. The end-caps electrodes have positive charge if the ions confined are positive. The main effect of the electric field is the shift of the ions toward the center of the trap; the force that acts toward the ion is proportional to the displacement of the ion in respect of the origin. This interaction results in harmonic oscillations of the ion along the axial direction. Due to the repulsive electric field along x- and y-direction the ion tends to be pushed out from the trap in the radial direction. As soon as the motion of the ion takes a the radial direction, due to the presence of the magnetic field, it is turned back along a cyclotron-type orbit. Studying the overall motion of the particle we can assume that the main motion is given by the harmonic component along the z-axis and the other two components of motion given by the cyclotron and magnetron drift motion (caused by the crossing of electric and magnetic field $E \times B$) again along z-axis. The result is a precessional motion in the equatorial plane around the z-axis.

The motion of an ion in a Penning trap is induced by the combination of the magnetic and electric field. For a constant electromagnetic field the vector potential A and the scalar potential ϕ can be chosen for a constant electric field as

$$A = 0 \tag{29}$$

$$\phi = \phi \tag{30}$$

and for a constant magnetic field

$$A = \frac{1}{2} B \times r \tag{31}$$

$$\phi = 0$$

For a mass m of the particle and for the potential as $(\phi, \frac{1}{2} B \times r)$ we obtain the Lagrangian

$$\begin{aligned} L &= \tfrac{m}{2}\dot{r}^2 + \tfrac{e}{2c}[r, r, B] - e\dot{\phi} + \int dV\, L_0 \\ &= \tfrac{m}{2}\left(\dot{x}^2 + \dot{y}^2 + \dot{z}^2\right) + \tfrac{eB}{2c}\left(x\dot{y} - y\dot{x}\right) - e\phi + \int dV\, L_0 \end{aligned} \tag{32}$$

where

$$\phi = \frac{U}{2z_0^2 + r_0^2}(-x^2 - y^2 + 2z^2) \tag{33}$$

and B points toward the positive direction of z-axis. The $\int dV\, L_0$ term is the field-free Lagrangian and can be neglected. Applying the Euler-Lagrange equation

$$\ddot{x} = \omega_c \dot{y} + \frac{1}{2}\omega_{0z}^2 x \tag{34}$$

$$\ddot{y} = -\omega_c \dot{x} + \frac{1}{2}\omega_{0z}^2 y \tag{35}$$

$$\ddot{z} = -\omega_{0z}^2 z \tag{36}$$

where we can define the *axial frequency* as

$$\omega_{0z} = \sqrt{\frac{4eU}{m\,(2z_0^2 + r_0^2)}} \tag{37}$$

and the *cyclotron frequency* as

$$\omega_c = \frac{eB}{mc} \tag{38}$$

At this point by using the equation (34) and the equation (35) and defining a new variable $u = x + iy$ the equation for the *radial motion* is obtained:

$$\ddot{u} = -i\omega_c \dot{u} + \frac{1}{2}\omega_{0z}^2 u \tag{39}$$

As said above the motion of each ion for this type of trap is the result of three different motions: axial, cyclotron motion and magnetron motion. These three motions are uncoupled and completely independent. Some examples of these complex motion are given in the figures 5 to **??**.

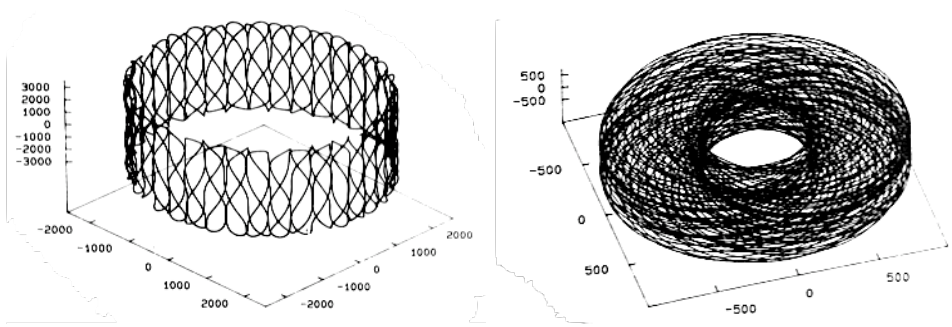

Figure 5. (left) Ion trajectory in Penning trap @ $B = 1T$, $U = 1V$, $r_0 = 5mm$. (right) Ion trajectory in Penning trap @ $B = 5T$, $U = 1V$, $r_0 = 1mm$.(Pradip K. Ghosh, Ion Traps, Clarendon Press, Oxford 1995)

III. System Configuration

Figure 6 shows the geometry under consideration for a 10 meter aperture in formation: the set of two rings in the lower part of the figure represents a double-ring electromagnetic confinement system, and the cylinder above represents the adaptive optics stage, with science camera. The top inflatable ring is empty inside, while the bottom inflatable ring is a torus which keeps the membrane with the electrode patches taut. The granular aperture is trapped in the space between the two electrode systems. The model in Figure 6 is obtained via finite elements, in which 168 triangle elements and 121 nodes form the membrane, 72 nodes in the bottom ring, 63 elements and nodes in the top ring. In the following, we analyze the two-dimensional and three-dimensional electrostatic stability of the cloud of granular matter, floated between the electrode rings.

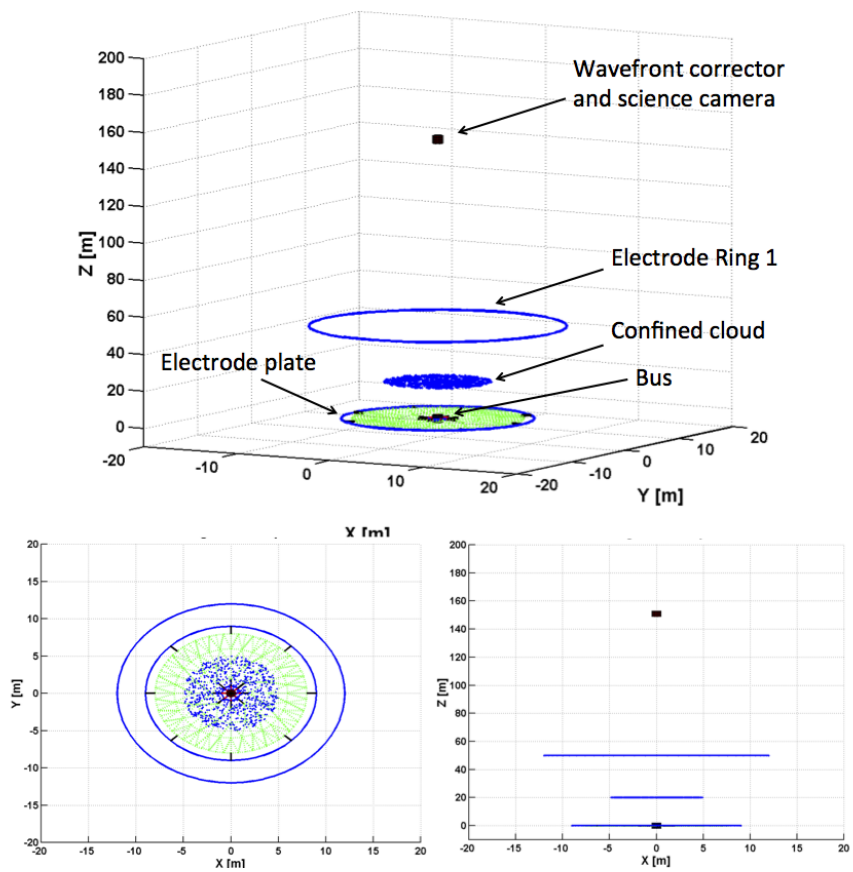

Figure 6. Prototype configuration for 10 meter Granular Imager with Electromagnetic confinement rings.

The two-dimensional geometry is a simplified trap model that is not sensitive to the stability problems due to the fact that it ignores the Earnshaw's theorem. Despite it doesn't have a strong correspondence to the real behavior of the charges/ions, it is still useful to understand how and why the charge moves along a given trajectory and what we can do to influence it.

The geometry (Fig.(7)) consists on two electrodes, one ring and one plate, positioned along the symmetry axis (x-axis) and other two electrodes positioned symmetrically with respect to the x-axis. The ring and the plate provide the constant electric field (DC) and the two others provide the radio frequency (RF).

Due to the two-dimensional analysis the ring is substituted by two dimensionless charges of the same value, so they generate a radial electric field named E_{21} and E_{22}. The plate is positioned in the origin (O) of the reference system and it generates an uniform electric field E_1 acting only along the in x-axis. The other two electrodes generate also an uniform and constant electric field (Variable EF) along the y-axis. In each couple of coordinate x-y it is possible to define the local electric field direction and magnitude by summing all the local contributes from each electrode. The model assumptions are that the ring is substituted by two dimensionless charges of the same value, that the plate generates an uniform and constant electric field

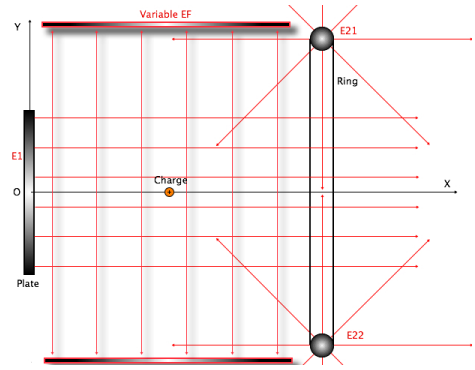

Figure 7. Two-dimensional geometry

along the x-axis, and that all the edge effects are neglected.

The three-dimensional geometry is a result of several improving steps that has been carried on during the trap design. The first tested trap was the two-dimensional one in which a z-axis was added. Working in a three-dimensional volume we decided to decouple the equations of motion organizing them in order to describe the resultant accelerations along each axis separately. The fixed points found in this configuration result to be unstable, so we decided to change it using firstly just two rings and than the classic paul trap configuration with two flat electrodes and one ring in the middle. It is possible to summarize all the design changes that has been made during the development:

The first geometry correspond to a three-dimensional version of the two-dimensional design: it has a single fixed point located between the two electrodes. The fixed point coordinate depend on the charge value of both the ring and the plate; in this case we have it at $x \cong 0.25$ (see Fig. (8)) where the sum of each electric field sources is zero. This fixed point is characterized by an unstable equilibrium: in fact while the x-components are null in this particular coordinate, the y- and z-components are not zero and tend to repulse the charge toward radial direction.

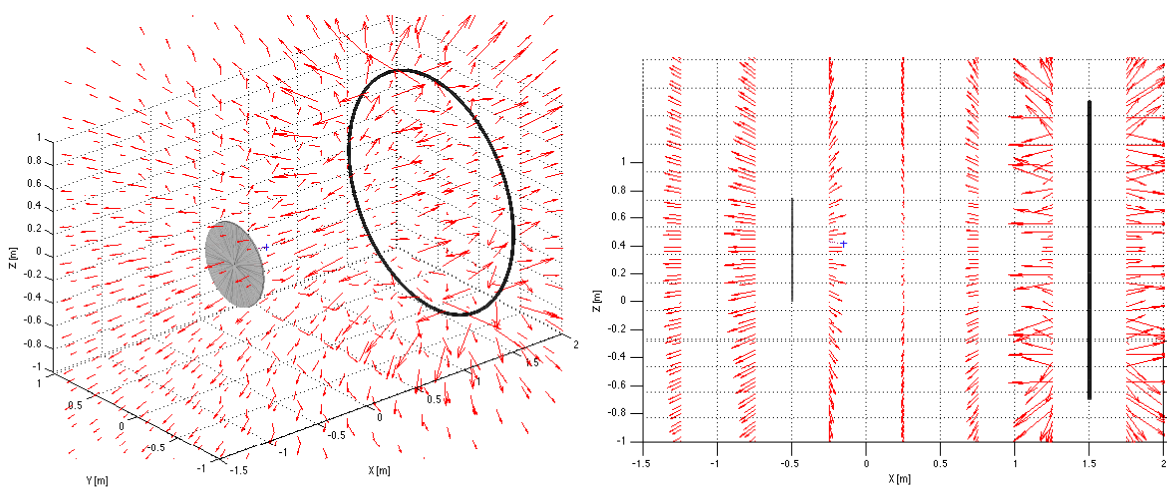

Figure 8. (left) First three-dimensional geometry configuration. (right) x-z plane view

The second design is represented by two concentric ring electrodes positioned along the x-axis (Fig.(9)). Initially the tests were conduced using two rings with the same size but the only things that follows the size change is the electric field pattern and not the nature of the fixed point(s) stability. Having two identical electrodes both of them positively and equally charged the fixed point is located between them along the x-axis.

Focusing on the electric field magnitude close to the center of the rings is well understood why the fixed point in the middle of the trap is unstable: the mutual influence between the two electrodes creates an y-z

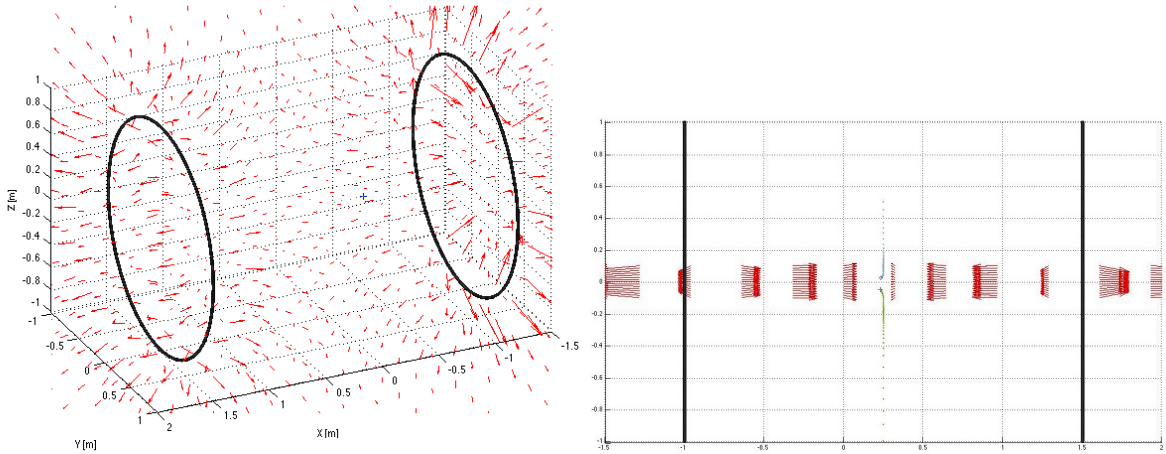

Figure 9. (left) Second three-dimensional geometry configuration. (right) x-z plane view.

plane at a certain x-coordinate ($x = 0.25$) in which all the forces and accelerations are null. Even though the charged particle in this particular x-coordinate lacks motion in the x-component, it has acceleration components that make the particle leave the trap along a trajectory that lies on the y-z plane (Fig.9).

By using an additional RF to overcome the Earnshaw's theorem it is possible to establish a dynamic stability similar to the one expressed by Mathieu equation, so this opportunity opens to new point of view regarding ion trapping. Focusing on the main purpose of this examination this design allows the development and control of optic devices due to the lack of plates in the light trajectory.

The third design is more similar to a regular electromagnetic trap. The introduction of a third electrode solves the stability problem recreating the same dynamics of a Paul trap. This trap is made by two end-caps electrodes or plates which can be shaped in order to obtain a particular electric field distribution, and a ring similar to what we used for the previous designs (Fig.(10)). This design is sensitive to the instability described by Earnshaw's theorem and it's electric fields are controlled in the same way a regular trap is driven.

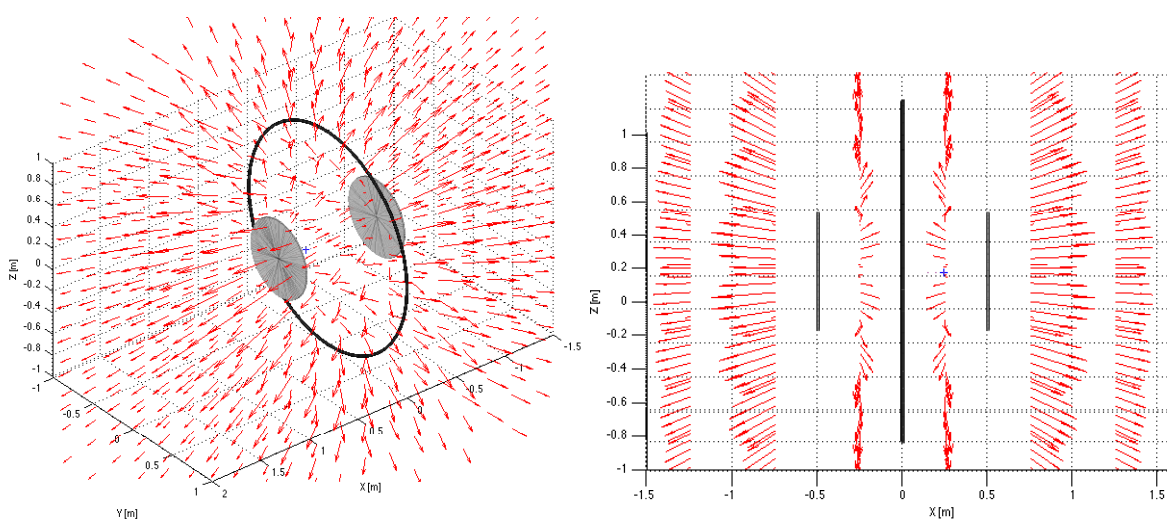

Figure 10. (left) Third three-dimensional geometry configuration. (right) x-z plane view.

The fixed point(s) is in this case kept successfully stable by a driven radio frequency (RF) and the position of this fixed point(s) can be changed by varying the electrodes parameters (gains, voltages, shape...). In the figure (10) the stable or unstable location of the fixed point(s) lies on the y-z plane.This marked customization lead us to the achievement of multiple cloud shapes in order to fit different purposes.

IV. Equations of Motion of Orbiting Granular Systems with Contact

Modeling of granular media in space is more challenging than modeling of conventional space-borne vehicles because we are faced with a probabilistic vehicle composed of a large number of physically disconnected grains. First, different scales of motion occur simultaneously in a cloud: translations and rotations of the cloud as a whole (macro-dynamics), relative rotation and translation of one cloud member with respect to another (meso-dynamics), and individual cloud member dynamics (micro-dynamics). A major challenge is to incorporate these modes of motion into a reduced order model. Related work in modeling and simulation of granular media is covered elsewhere,[5],[7],[14],[?] and in.[18] By means of micro-continuum field theory,[?] we can unify the deformation and dynamics modalities of a cloud. We use continuum mechanic constructs for this analysis. Each individual grain is endowed with a position vector, a rotation tensor, and a deformation gradient tensor, in the spirit of micromorphic kinematics. This means that each individual grain is capable of changing its configuration in response to stimuli originated either from the exterior of the cloud or within the cloud itself. The cloud is therefore treated as a continuum at the macroscopic level, with added extra structure at the micro-continuum, or particle, level. In space, the cloud behavior depends on the dynamic balance of different force fields: Laser light pressure, as light can induce motion; Solar illumination radiation pressure, which carries momentum; Gravitational forces and gradients, resulting in orbital and tidal effects; Electrostatic Coulomb or dielectrophoretic forces, since the grains are charged; Electromagnetic Lorentz forces resulting from the interaction with local magnetic field; Cloud self-gravity caused by the cloud being an extended body; Poynting-Robertson drag, in which grains tends to spiral down towards the Sun; and Yarkovstky (YORP) effect, caused by the anisotropic emission of thermal photons, which carry momentum. A small particle in the presence of light will experience both a scattering force in the direction of the beam axis, which is proportional to the irradiance, and a gradient force that may be expressed as $F_{grad} = -\frac{1}{2}\alpha\nabla\mathbf{E^2}$, where α is the polarizability of the particle.[1] The gradient force is the direction of the beam axis is negligible unless the beam is tightly focus. Beam shaping of a cloud of particles is possible by molding the cloud in with the gradient force, say in the x-y plane, and by further molding the cloud in the z-direction by the combined optical scattering force and gravitational forces arising from the orbital dynamics (tidal forces). Relevant work is presented in,[22],[21],[16] and in.[12] Cloud reorientation is discussed in.[13] Applications to telescopes are discussed in,[10],[8].[9] Relevant control techniques can be examined in[20] and in.[19]

The equations of motion of the entire system will be derived in this section. An inertial reference frame $\mathcal{F}_I$ is defined by the X-axis along the vernal equinox, the Z-axis along the direction of the system's angular momentum, and the Y-axis completes the right-handed triad. The origin of $\mathcal{F}_I$ is placed at the center of the Earth's geocentric frame. The position and velocity of the center of mass of bodies i and j (also representing nodes i and j of an extended finite element body) is given by vectors $\mathbf{r}_i$ and $\mathbf{r}_j$, and $\dot{\mathbf{r}}_i$ and $\dot{\mathbf{r}}_j$ respectively measured from the origin of $\mathcal{F}_I$. Similarly, the attitude of the reference frames $\mathcal{F}_i$ and $\mathcal{F}_j$ of bodies i and j with respect to the inertial frame $\mathcal{F}_I$ is described by tensors $\mathbf{A}_i$ and $\mathbf{A}_j$, and their angular velocity by vectors ω_i and ω_j, respectively. We parameterize the translation of body i by the components of vectors $\mathbf{r}_i$ and $\dot{\mathbf{r}}_i$ in $\mathcal{F}_I$, and its rotation with respect to $\mathcal{F}_I$ by the quaternion parameters $\mathbf{q}_i$ and the angular velocity ω_i. We introduce the orbiting reference frame $\mathcal{F}_{ORF}$, which we use to describe the near field dynamics of the spacecraft relative to its orbit. This reference frame is attached to a point that follows a Keplerian orbit around the primary body. $\mathcal{F}_{ORF}$ is defined by the direction of the orbital velocity vector (x-axis), the local vertical (z-axis), and the orbit normal (y-axis). The orbit of the origin of $\mathcal{F}_{ORF}$ is defined by the six orbital elements a (semimajor axis), e (eccentricity), i (inclination), Ω_l (longitude of ascending node), ϖ (argument of perigee), ν (true anomaly), and time of passage through perigee. The orbital radius is R_0, and the orbital angular velocity vector is denoted by $\mathbf{\Omega}$. The transformation between $\mathcal{F}_{ORF}$ and $\mathcal{F}_I$ is given by $\mathcal{F}_{ORF} = \mathbf{R}\mathcal{F}_I$, where $\mathbf{R}_i(\cdot)$ denotes a rotation matrix of $(\cdot)$ around the direction specified by the subscript. $\mathbf{R}$ depends on ϖ, ν, i, and Ω_l. It is useful to refer the translational dynamics of body i to the origin of $\mathcal{F}_{ORF}$.

In Chrono::Engine,[3] DVI (Differential Variational Inequality) formulations are used for non-smooth dynamics, and explicit or implicit integrators are used for ODE and DAE. In the field of classical smooth dynamics, there are Ordinary Differential Equations (ODE) and Differential Algebraic Equations (DAE). In the non-smooth dynamics instead, unilateral rigid contacts between parts are considered and therefore Differential Variational Inequalities (DVI) come out. They are also called Measure Differential Inclusions (MDI). In any case, DVI provide a generalization to ODE and DAE. In classical ODE and DAE, smooth accelerations, speeds and positions are assumed. If hard contacts are considered, they lead to non-smooth trajectories, creating jumps in speeds. This can be avoided by introducing non-smooth dynamics. Impact

events can be considered as impulsive phenomena, and therefore acceleration contains a certain number of spikes and it has to be considered using the theory of measures. In the theory, accelerations $\nu(t)$ are introduced using distributions, speeds $v(t)$ are functions of Bounded Variation, and positions $\mathbf{q}(t)$ are absolutely continuous functions. We now consider an element of a granular medium as a rigid body subject to contact and collisions. The state of a mechanical system with n_b rigid bodies in three dimensional space can be represented by the generalized positions $\mathbf{q} = [{r_1}^T, {\epsilon_1}^T, \ldots, {r_{n_b}}^T, {\epsilon_{n_b}}^T]^T \in \mathbb{R}^{7n_b}$ and their time derivatives $\dot{\mathbf{q}}$, where r_i is the absolute position of the center of mass of the $i-th$ body and the quaternion ϵ_i expresses its rotation. One can also introduce the generalized velocities $\mathbf{v} = [{r_1}^T, {\omega_1}^T, \ldots, {r_{n_b}}^T, {\omega_{n_b}}^T]^T \in \mathbb{R}^{7n_b}$, directly related to $\dot{\mathbf{q}}$ by means of the linear mapping $\dot{\mathbf{q}} = \mathbf{L}(\mathbf{q})\mathbf{v}$ that transforms each angular velocity (expressed in the local coordinates of the body) into the corresponding quaternion derivative $\dot{\epsilon_i}$ by means of the linear algebra formula $\dot{\epsilon_i} = \frac{1}{2}G(\epsilon_i)\omega_i$, where $G(\epsilon_i$ is a nonlinear operator function of the quaternion parameters. Mechanical constraints translate into algebraic equations that constrain the relative position of pairs of bodies. Assuming a set of constraints is present in the system, for all $i \in \mathcal{B}$ they lead to the scalar equations $\Psi_i(\mathbf{q}, \mathbf{t}) = \mathbf{0}$. To ensure that constraints are not violated in terms of velocities, one must also satisfy the first derivative of the constraint equations, that is $\nabla {\Psi_i}^T \mathbf{v} + \frac{\partial \mathbf{\Psi_i}}{\partial \mathbf{t}} = \mathbf{0}$ with the Jacobian matrix $\nabla_q \Phi_i = [\partial \Psi_i / \partial \mathbf{q}]^{\mathbf{T}}$ and $\partial {\Phi_i}^T = \nabla_{\mathbf{q}} {\Psi_i}^T \mathbf{L}(\mathbf{q})$. If contacts between rigid bodies must be taken into consideration, colliding shapes must be defined for each body, and a collision detection algorithm must be used to provide a set of pairs of contact points for bodies whose shapes are near enough, so that a set $\mathcal{A}$ of inequalities can be used to concisely express the non-penetration condition between the volumes of the shapes, i.e. for all $i \in \mathcal{A}$, $\Phi(\mathbf{q}) \geq \mathbf{0}$. Given two bodies in contact $\mathcal{A}, \mathcal{B}$, let n_i be the normal at the contact pointing toward the exterior of body $\mathcal{A}$, and let $\mathbf{u_i}$ and $\mathbf{w_i}$ be two vectors in the contact plane such that $\mathbf{n_i}, \mathbf{u_i}, \mathbf{w_i} \in \mathbb{R}^{\mathbf{3}}$ are mutually orthogonal vectors: when a contact i is active, that is for $\Phi(\mathbf{q}) = \mathbf{0}$, the frictional contact force act on the system by means of multipliers $\hat{\gamma}_{i,n} \geq 0$, $\hat{\gamma}_{i,u}$, and $\hat{\gamma}_{i,w}$, that is the normal component of the contact force acting on body $\mathcal{B}$ is $\mathbf{F_{i,N}} = \hat{\gamma}_{\mathbf{i,n}} \mathbf{n_i}$ and the tangential component is $\mathbf{F_{i,T}} = \hat{\gamma}_{\mathbf{i,u}} \mathbf{u_i} + \hat{\gamma}_{\mathbf{i,w}} \mathbf{w_i}$ (for body $\mathcal{B}$ these forces have the opposite sign). Also, according to the Coulomb friction model, in case of nonzero relative tangential speed $\mathbf{v_{i,T}}$ the direction of the tangential contact force is aligned with $\mathbf{v_{i,T}}$ and it is proportional to the normal force as $\parallel \mathbf{F_{i,T}} \parallel = \mu_{\mathbf{i,d}} \parallel \mathbf{F_{i,N}} \parallel$ by means of the dynamic friction coefficient $\mu_{i,d} \in \mathbb{R}^+$. However, in case of null tangential speed, the strength of the tangential force is limited by the inequality $\parallel \mathbf{F_{i,T}} \parallel \leq \mu_{\mathbf{i,s}} \parallel \mathbf{F_{i,N}} \parallel$ using a static friction coefficient $\mu_{i,s} \in \mathbb{R}^+$., and its direction is one of the infinite tangents to the surface. In our model we assume that $\mu_{i,s}$ and $\mu_{i,d}$have the same value that we will write μ_i for simplicity, so the above mentioned Coulomb model can be stated succinctly as $\hat{\gamma}_{i,n} \geq 0, \quad \Phi_i(\mathbf{q}) \geq \mathbf{0}, \quad \mathbf{\Phi_i}(\mathbf{q})\hat{\gamma}_{\mathbf{i,n}} = \mathbf{0}$. This implies three conditions. The first condition states that the friction force is always within the friction cone. The second condition states that the friction force and the velocity between two contacting bodies are collinear and of opposite direction. The third condition captures the stick-slip transition. Note that the condition $\hat{\gamma}_{i,n} \geq 0, \quad \Phi_i(\mathbf{q}) \geq \mathbf{0}, \quad \mathbf{\Phi_i}(\mathbf{q})\hat{\gamma}_{\mathbf{i,n}} = \mathbf{0}$ can be also written as a complementarity constraint: $\hat{\gamma}_{i,n} \geq 0, \quad \Phi_i(\mathbf{q}) \geq \mathbf{0}$. This model can also be interpreted as the Karush-Kuhn-Tucker first order conditions of an equivalent maximum dissipation principle. Finally, we must also consider the effect of external forces with the vector of generalized forces $\mathbf{f}(\mathbf{t}, \mathbf{q}, \mathbf{v}) \in \mathbb{R}^{\mathbf{6n_b}}$, that might contain gyroscopic terms, gravitational effects, forces exerted by springs or dampers, torques applied by motors, and so on. Considering the effects of both the set $\mathcal{A}$ of frictional contacts and the set $\mathcal{B}$ of bilateral constraints, the system cannot be reduced neither to an ordinary differential equation (ODE) of the type $\dot{v} = \mathbf{f}(\mathbf{t}, \mathbf{q}, \mathbf{v})$ nor to a differential-algebraic equation (DAE), because of the inequalities and because of the complementarity constraints, that rather turn the system into a differential inclusion of the type $\dot{v} \in \mathcal{F}(\sqcup, \mathbf{q}, \mathbf{v})$, where $\mathcal{F}$ is a set-valued multifunction. In fact, the time evolution of the dynamical system is governed by the following equations, i.e., the kinematic geometry conditions:

$$\dot{\mathbf{q}} = \mathbf{L}(\mathbf{q})\mathbf{v} \tag{40}$$

the kinematic constraint equations:

$$i \in \mathcal{B}: \qquad \Psi_i(\mathbf{q}, \mathbf{t}) = \mathbf{0} \tag{41}$$

and the complementarity conditions:

$$i \in \mathcal{A}: \qquad \hat{\gamma}_{i,n} \geq 0, \perp \Phi_i(\mathbf{q}) \geq \mathbf{0}, \quad , (\hat{\gamma}_{\mathbf{i,u}}, \hat{\gamma}_{\mathbf{i,w}}) \underset{\mu_{\mathbf{i}}\hat{\gamma}_{\mathbf{i,n}} \geq \sqrt{\hat{\gamma}^{\mathbf{2}}_{\mathbf{i,u}} + \hat{\gamma}^{\mathbf{2}}_{\mathbf{i,w}}}}{\mathbf{argmin}} \mathbf{v^T}(\hat{\gamma}_{\mathbf{i,u}}\mathbf{D_{i,u}} + \hat{\gamma}_{\mathbf{i,w}}\mathbf{D_{i,w}})) \tag{42}$$

Measuring translational quantities with respect to $\mathcal{F}_{ORF}$, the translation kinematics and dynamics equations of a point mass of mass m in a general orbit are:

$$\ddot{\rho}_i = -\ddot{\mathbf{R}}_0 - \mathbf{\Omega} \times \mathbf{\Omega} \times \rho_i - 2\mathbf{\Omega} \times \dot{\rho}_i + \mathbf{R}\ddot{\mathbf{r}}_i(nearfield) \tag{43}$$

with

$$\ddot{\mathbf{r}}_i = -\mu_E \frac{\mathbf{r}_i}{\mathbf{r}_i^3} + \frac{\mathbf{f}_a + \mathbf{f}_S + \mathbf{f}_e}{m_i}(farfield) \tag{44}$$

and

$$\ddot{\mathbf{R}}_0 = -\mu_E \frac{\mathbf{R}_0}{\mathbf{R}_0^3} + \frac{\mathbf{f}_{pert} + \mathbf{f}_S + \mathbf{f}_e}{m_i}(farfield) \tag{45}$$

where: ρ = relative position vector of mass with respect to ORF, R_0 = orbital radius vector to origin of ORF, Ω = orbital rate, μ_E = gravitational parameter, f_a = thruster actuation force vector, f_S = solar pressure force vector, f_3 = third-body forces vector, m = grain mass , and f_{pert}= resultants of higher order gravitational terms from the primary acting on the entire system as an extended body.

With the kinematics and kinetics above, the system momentum balance becomes:

$$\mathbf{M}\dot{\mathbf{v}} = \mathbf{f}(\mathbf{t}, \mathbf{q}, \mathbf{v}) + \sum_{\mathbf{i} \in \mathcal{B}} \hat{\gamma}_{\mathbf{i,n}} \nabla \mathbf{\Psi_i} + \sum_{\mathbf{i} \in \mathcal{A}} (\hat{\gamma}_{\mathbf{i,n}} \mathbf{D_{i,n}} + \hat{\gamma}_{\mathbf{i,u}} \mathbf{D_{i,u}} + \hat{\gamma}_{\mathbf{i,w}} \mathbf{D_{i,w}})) \tag{46}$$

As an example, the set of equations of motion for one unconstrained grain subject to boundary electric fields are as follows:

$$\begin{aligned}
\frac{d^2x}{dt} &= \frac{F_{x0}}{m} + \\
&+ C\frac{dx}{dt} + \\
&+ \frac{Q}{m}\Bigg[A_1\left(\frac{Q_{plate1}}{4\pi\varepsilon_0}\frac{1}{(r-r_{P1})^2}\right)_x + A_2\left(\frac{Q_{plate2}}{4\pi\varepsilon_0}\frac{1}{(r-r_{P2})^2}\right)_x + \\
&+ A_3\left(\frac{Q_{plate1}}{4\pi\varepsilon_0}\frac{1}{(r-r_{P1})^2}\right)_x \sin(\omega_{Px}t + \varphi_x) + A_4\left(\frac{Q_{plate2}}{4\pi\varepsilon_0}\frac{1}{(r-r_{P2})^2}\right)_x \sin(\omega_{Px}t + \varphi_{Px}) + \\
&+ A_5\left(\frac{Q_{ring}}{4\pi\varepsilon_0}\frac{1}{(r-r_r)^2}\right)_x \cos\left(\arctan\left(\frac{d}{2r}\right)_x\right) + \\
&+ A_6\left(\frac{Q_{ring}}{4\pi\varepsilon_0}\frac{1}{(r-r_r)^2}\right)_x \cos\left(\arctan\left(\frac{d}{2r}\right)_x\right)\sin(\omega_{Rx}t + \varphi_{Rx}) + \\
&+ E_{x_{MAX}}\frac{\sigma_{plate1}}{2\varepsilon_0}\sin(\omega_{Ex}t + \varphi_{Ex}) \\
&+ E_{x_{MAX}}\frac{\sigma_{plate2}}{2\varepsilon_0}\sin(\omega_{Ex}t + \varphi_{Ex})\Bigg]
\end{aligned}$$

$$\begin{aligned}
\frac{d^2y}{dt} &= \frac{F_{y0}}{m} + \\
&+ C\frac{dy}{dt} \\
&+ \frac{Q}{m}\Bigg[A_1\left(\frac{Q_{plate1}}{4\pi\varepsilon_0}\frac{1}{(r-r_{P1})^2}\right)_y + A_2\left(\frac{Q_{plate2}}{4\pi\varepsilon_0}\frac{1}{(r-r_{P2})^2}\right)_y + \\
&+ A_3\left(\frac{Q_{plate1}}{4\pi\varepsilon_0}\frac{1}{(r-r_{P1})^2}\right)_y \sin(\omega_{Px}t + \varphi_x) + A_4\left(\frac{Q_{plate2}}{4\pi\varepsilon_0}\frac{1}{(r-r_{P2})^2}\right)_y \sin(\omega_{Pyz}t + \varphi_{Pyz}) + \\
&+ A_5\left(\frac{Q_{ring}}{4\pi\varepsilon_0}\frac{1}{(r-r_r)^2}\right)_y \cos\left(\arctan\left(\frac{d}{2r}\right)_y\right) + \\
&+ A_6\left(\frac{Q_{ring}}{4\pi\varepsilon_0}\frac{1}{(r-r_r)^2}\right)_y \cos\left(\arctan\left(\frac{d}{2r}\right)_y\right)\sin(\omega_{Ryz}t + \varphi_{Ryz}) + \\
&+ E_{y_{MAX}}\sin(\omega_{Ey}t + \varphi_{Ey})]
\end{aligned}$$

$$\begin{aligned}
\frac{d^2z}{dt} &= \frac{F_{z0}}{m} + \\
&+ C\frac{dz}{dt} \\
&+ \frac{Q}{m}\Bigg[A_1\left(\frac{Q_{plate1}}{4\pi\varepsilon_0}\frac{1}{(r-r_{P1})^2}\right)_z + A_2\left(\frac{Q_{plate2}}{4\pi\varepsilon_0}\frac{1}{(r-r_{P2})^2}\right)_z + \\
&+ A_3\left(\frac{Q_{plate1}}{4\pi\varepsilon_0}\frac{1}{(r-r_{P1})^2}\right)_z \sin(\omega_{Px}t + \varphi_x) + A_4\left(\frac{Q_{plate2}}{4\pi\varepsilon_0}\frac{1}{(r-r_{P2})^2}\right)_z \sin(\omega_{Pyz}t + \varphi_{Pyz}) + \\
&+ A_5\left(\frac{Q_{ring}}{4\pi\varepsilon_0}\frac{1}{(r-r_r)^2}\right)_z \cos\left(\arctan\left(\frac{d}{2r}\right)_y\right) + \\
&+ A_6\left(\frac{Q_{ring}}{4\pi\varepsilon_0}\frac{1}{(r-r_r)^2}\right)_z \cos\left(\arctan\left(\frac{d}{2r}\right)_y\right)\sin(\omega_{Ryz}t + \varphi_{Ryz}) + \\
&+ E_{z_{MAX}}\sin(\omega_{Ez}t + \varphi_{Ez})]
\end{aligned}$$

V. Numerical experiments

A. Model Validation

The correctness of trajectory integration process can be checked by monitoring the RF amplitude and its frequency at which the particle sitting close to the center of the trap becomes unstable. In the case where pure RF excitation is applied to the ring electrode, stability limit is marked by the Mathieu parameter value q = 0.908. This is a theoretical result for an ideal Paul trap. For the practical Paul traps, ions might get ejected at slightly lower or higher value. The phenomenon is referred as early and delayed ejection respectively. The consistence of the new implemented model is confirmed by comparing the simulation results to the ones which are already demonstrated. Three examples are reported: the figure 11 represent the comparison of two ion trajectories, one is obtained from the new mathematical model and the second comes from a Master degree thesis of the Indian Institute of Science.[23] The trajectories are similar even though the magnitude of the motion is different. The parameters set for this simulation are shown in the table (3).

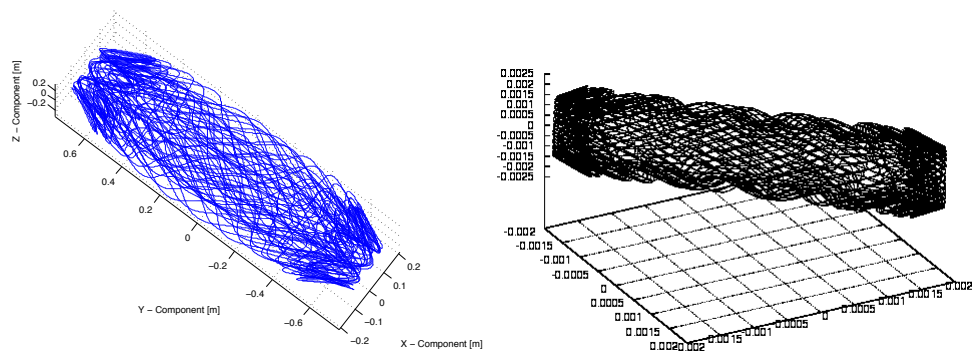

Figure 11. Trajectory of a charge simulated on MATLAB using the new mathematical model (left), ion trajectory from[23]" (right)

Parameter	*Value*
Q	1e-13
m	1e-13
U	5e-5
V	0.1
OMEGA	1.1

Table 3. Parameters set for the figure (11)

The figures (12) and (13) show the comparison of two pictures from[6] and the trajectory of a charged particle simulated trough the new mathematical model. The figure (13) is the result of the simulation parameters set reported in the table (4).

Parameter	*Value*
Q	1e-13
m	1e-13
U	5e-5
V	0.1
OMEGA	1

Table 4. Parameters set for the figure (13)

From the results we have seen it is possible to conclude that the final shape of the charged cloud of particles depends strictly on the imposed border conditions (U,V,$OMEGA$, q_n...). The most interesting

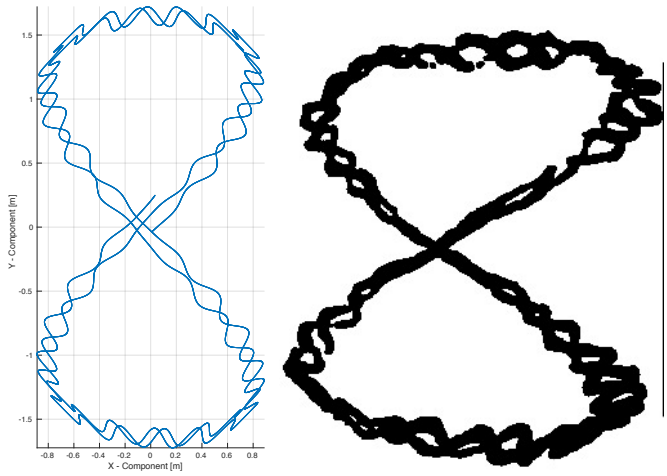

Figure 12. Trajectory of a charge simulated on MATLAB using the new mathematical model (left), trajectory taken from[6]"

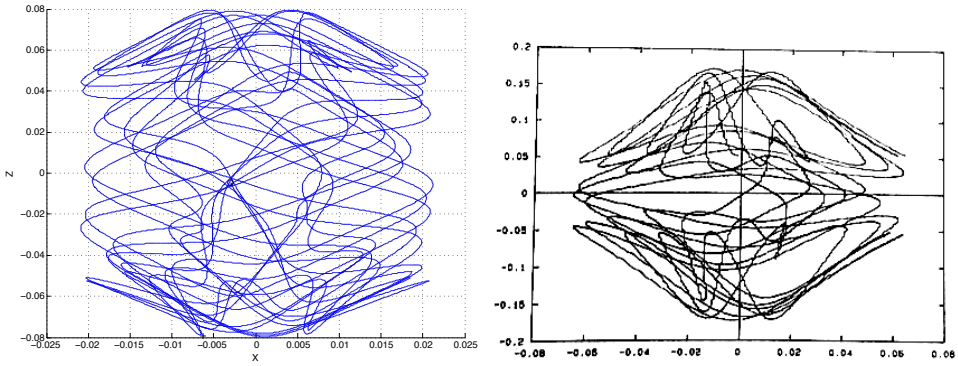

Figure 13. Trajectory of a charge simulated on MATLAB using the new mathematical model (left), trajectory taken from "Pradip K. Ghosh, Ion Traps[6]". All the dimensions are expressed in meters [m].

configuration are the ones described in the section (2) and section (3): the first one doesn't have plates and this means the light can pass trough the two rings or can be reflected without obstacles making the concept easy to realize and control. The second configuration is the classic Paul trap design so its behavior is well known. The kay factor is the possibility to reproduce an annulus made of charged particles that can be used as a reflecting medium despite the presence of the electrode. There is also the possibility to use a grid plate electrode: this can be a great solution in order to solve the main problem of having an opaque plate electrode. Having a grid in fact the light is allowed to pass trough the plate without any change or deviation while the electric field produced can be exact the same depending on the grid density.

An alternative solution may be the realization of an alternative charged structure which can be used as electrode that produces the same potential pattern of the charged plate. There will be a most convenient grid density (optimization point) that will balance the grid density and the light intensity that hits the cloud.

B. Experiments with rings and plates

1. Configuration with two electrodes: one ring and one plate

Multiple tests confirm that the configuration with a plate and a ring tends to be unstable and the ions escape the trap.

All the electric forces are in the same direction because there is no null force spot along the x-axis. The maximum electric field that comes from the ring is still lower than the one that comes from the plate, therefore there is no stability.

2. Configuration with two electrodes: two rings

This configuration gives a good stability margin when the RF is appropriately applied. Having two rings guarantees the location of the fixed point in the center of the trap if they have the same electrostatic charge. In fig. 14 we have two ring positioned respectively at $x = -1m$ and $x = 1m$, so the the fixed point where the two potentials match and erase each other is on the center of the trap in $x = 0m$.

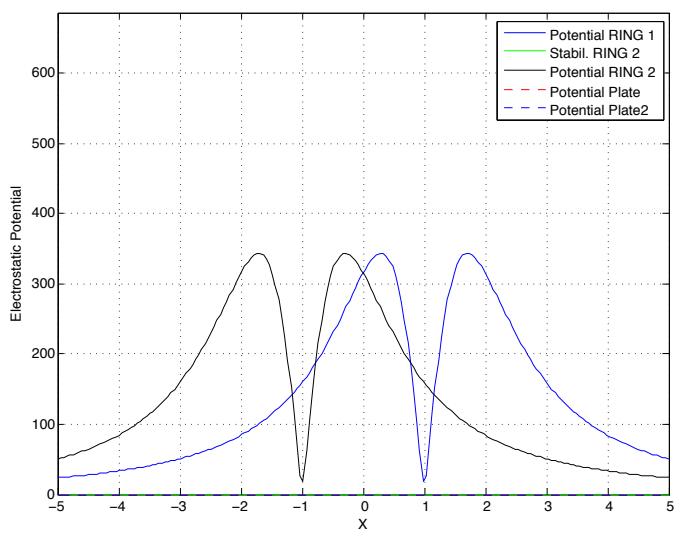

Figure 14. Electrostatic potential [V] along the x-axis [m]. The position of the two rings are $x = -1m$ and $x = 1m$

In order to maintain the charge in the center of the trap it is necessary to set the right parameters. If the conditions are not respected all the ions will leave the trap after a certain period (Fig.(15)) dependent on the potential value and the charge magnitude of the particle. The evolution of the x-, y-, z-components is reported in the figure (15) and shows how rapidly two of the three charges leave the trap increasing their velocity.

A second simulation reports the trapping of three ions using the two-ring configuration. The resultant trajectories, as we will see, are similar to the ones obtained with the Mathieu model and they can be easily

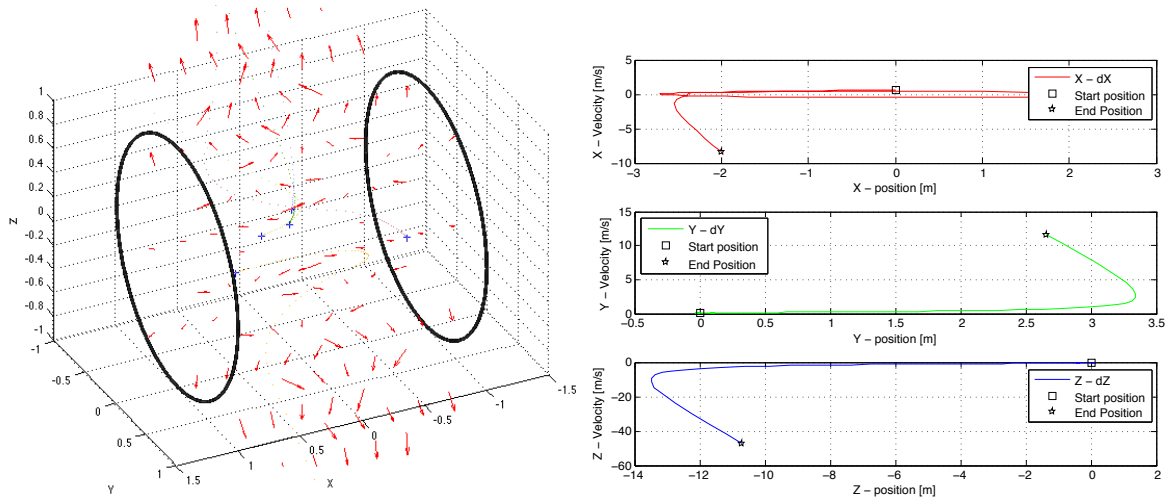

Figure 15. (left) Two ring configuration test, low RF. (right) Evolution of the motion in x-, y- and z-component, static EF and RF are applied.

controlled by change the ring parameters and the RF. The parameters used in the following simulation are described in the table (16).

The result is shown in the figure (17) where all the particles tend slowly ($C = 0.1$) to reach the fixed point in the center of the trap. The phase planes are shown in figure (17) and are again comparable with the Mathieu mathematical model. We can recognize two main frequencies: an high-frequency micro-motion and a secular low-frequency motion as the trapping theory predict. Sometimes the evolution in time is not perfectly regular due to the interference with the motion of the oter particles.

The Phase diagrams for the two given particles demonstrate the capability of the trap to maintain low average velocities and bounded x-, y-, z-positions.

3. Configuration with three electrodes: one ring, two plates (first parameter set)

The following configuration is similar to a classic Paul trap. The electrodes are set as hemispherical (see table (16)) and for certain conditions and parameters we can achieve different shapes of the final arrangement of the particles. Using specific conditions it is possible to achieve different particle distributions: two tests have been carried out using the settings reported in table (16).

These settings lead to a final stabile *annulus* pattern where the single particles keep moving just along the y- and z-axis in a *limit cycle* while their x-coordinate is constantly $x = 0$. For a better explanation can be useful to observe the phase figures (18), where one can notice the quick response of the x-component that reach the equilibrium position with few oscillations, while a limit cycle is established along the other two axes. A better view is given by the figure (18) which shows in particular the frequency of the two cycles.

More simulation have been done getting the same results; when the number of particle rises it is more clear the final annulus shape as the figure (19) shows.

4. Configuration with three electrodes: one ring, two plates (second parameter set)

Changing some key parameters (see Tab.(16)) it is possible to achieve the classic Paul trap ions trajectories, an example is shown in the figure (19). The final position of the ions in this case form a cusp-like shape that can be modified by varying parameters such RF or electrodes charge values.

All the ions are trapped and tend to reach the fixed point at the center of the trap ($C \neq 0$) if there was no damping all the particles would move close to the fixed point achieving a dynamic equilibrium. Studying one of these trapped particles it is possible to notice again two frequency components on the trajectory (Fig.(19)), the high frequency micro-motion and the low-frequency motion. Looking at the phase diagrams the motion is well bounded and both velocity and position tend slowly to reach the designed position.

Description	Two-rings	One ring two plates 1	One ring two plates 2
Ring diameter [m]	2	2	2
Number of particles	3	3	5
Ring-plate distance [m]	2	-	-
Ring half thickness (radius) [m]	0.01	0.01	0.01
Plate 1 position [m]	-	[-0.25,0.0]	[-0.25,0.0]
Plate 2 position [m]	-	[+0.25,0.0]	[+0.25,0.0]
Ring position [m]	-	[0,0,1]	[0,0,1]
Hemispherical electrode radius 1 [m]	-	1	1
Hemispherical electrode radius 2 [m]	-	1	1
Plate 1 diameter [m]	-	0.7	0.7
Plate 2 diameter [m]	-	0.7	0.7
Plate charge [C]	3e-7	-	-
Plate 1 charge [C]	-	1e-7	1e-10
Plate 2 charge [C]	-	1e-7	1e-10
Ring 1 charge [C]	1e-7	1.5e-7	1e-7
Ring 2 charge [C]	1e-7	-	-
Particle charge [C]	1e-13	1e-13	1e-13
Particle mass kg]	1e-13	1e-13	1e-13
Main ring DC gain	0.1	0	0
Optional ring DC gain	0.1	0	0
Stabilizer ring DC gain	0	0.1	0.1
Plate 1 DC gain	0	0.1	0.1
Plate 2 DC gain	0	0.1	0.1
Frequency of ring RF voltage [rad/s]	65	35	35
Frequency of plate 1 RF voltage [rad/s]	0	35	39
Frequency of plate 2 RF voltage [rad/s]	0	35	39
Amplitude of ring RF voltage	1.75	0.75	0.75
Damping constant	0.1	10	0.1
Plasma temperature [K]	300	300	300

Figure 16. Simulation parameters for case with two-rings, and case with one ring and two plates (models 1 and 2).

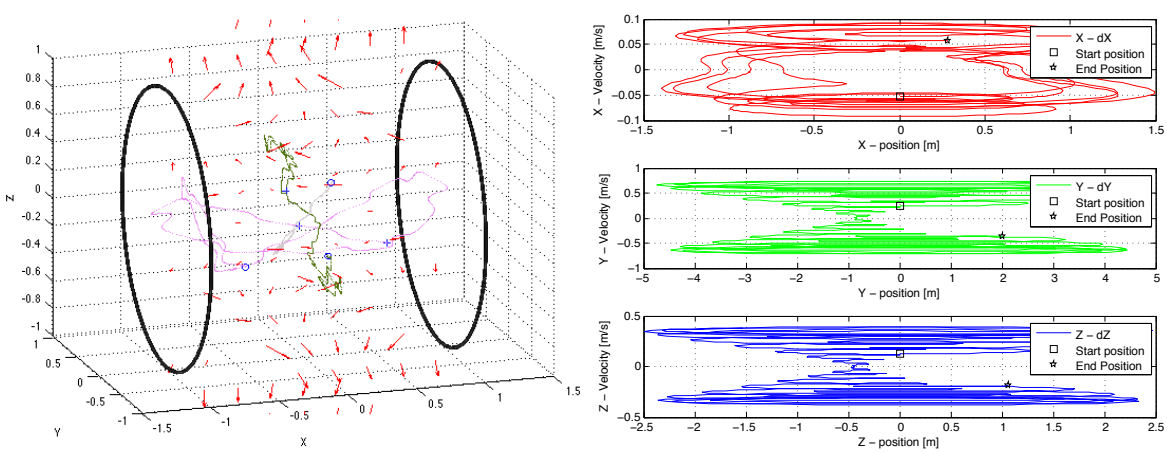

Figure 17. (left) Trapped particle trajectory. (right) Two-ring trap phase diagrams.

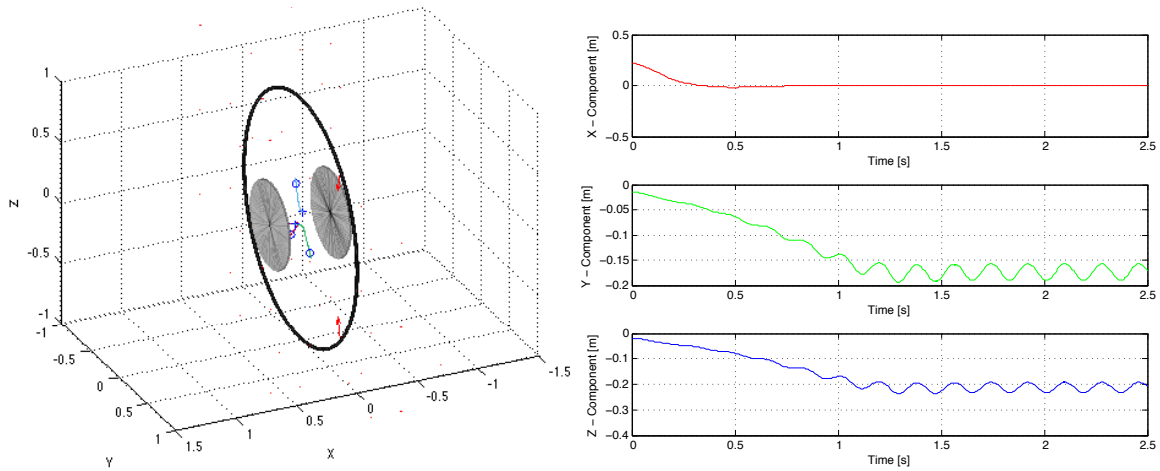

Figure 18. (left) 3 particles Paul-trap simulation. (right) Motion evolution in x-, y-, z-component.

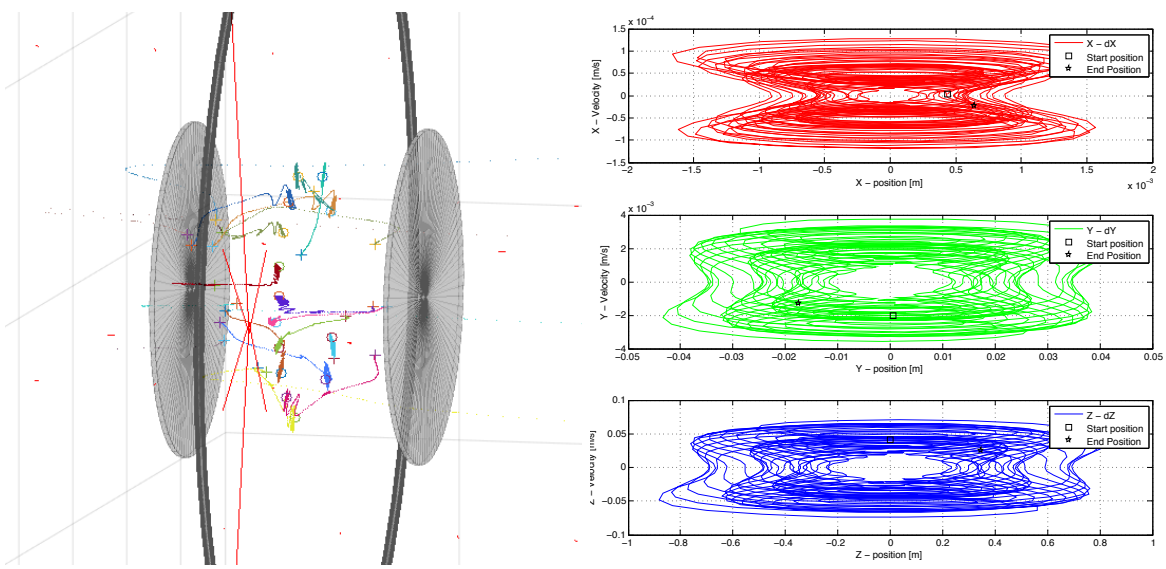

Figure 19. (left) 15 particles simulation. (right) Phase plane diagrams.

C. Example of cloud containment by equivalent fans

The next example is related to a first attempt to trap particles in an environment without gravity subjected to an initial random velocity. In order to do that six fans have been used, two per every direction and the particle whose behavior is under investigation is a sphere.

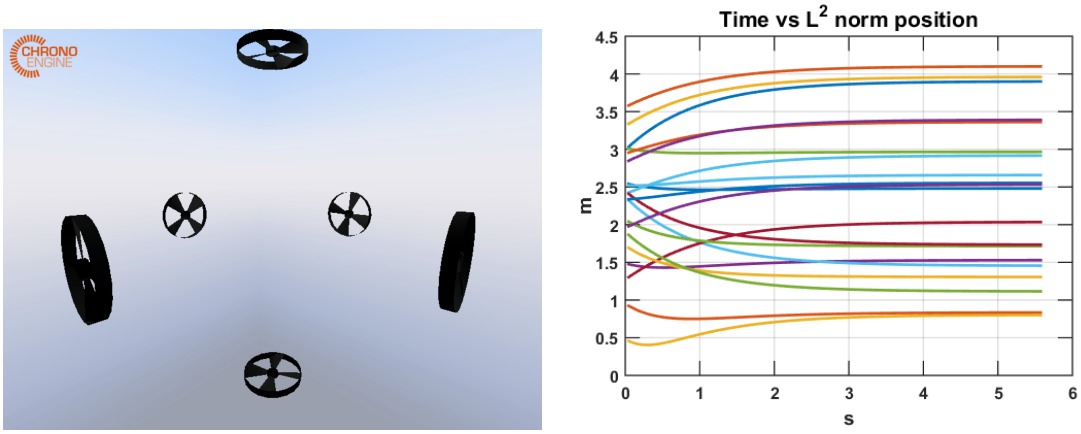

Figure 20. (left) Trapping system. (right) L2-norm of particles position

In this case, even if the goal of the present work is to trap particles throughout electromagnetic force fields, they have been used fans since as a first attempt "rough" wind forces has been considered. One of those is present in one of the tutorial on[?] and explain well how to manage rotations and force field in Chrono::Engine. The force applied to each body is function of their velocity v_i and of two constants, the speed of the wind v_w and the density of the mean ρ:

$$F = (v_w - v_i)\ \rho \tag{47}$$

In the Chrono simulator, these forces can be treated as functions acting on the bodies, depending on their states. The most interesting things to notice in previous figures are that the particle reaches a steady-state condition, and in particular, the particle is stopped and fixed in the space by the force field. In one simulation set with 20 particles, with the same module for initial velocities and angular velocities, but different origin in the space, the same behavior is shown in Fig. 20. Considering almost the same starting point for every simulation, it is interesting to analyze the distance covered by the particle before it is stopped by the force field. The most important parameter is Δposition, and it indicates how much space is needed to the force field generated by the fans to stop the particle movement. If one looks at the "Time Vs velocity vector" in Fig. 20 sees that the system can be modeled as a first order dynamical system. They are characterized by 48, a first order differential equation. In this case, x is equal to the velocity, the variable that actually is going to zero because of the force applied (as a consequence, position is going to asymptotically stabilize and acceleration is going to zero).

$$\dot{\mathbf{x}} + \frac{1}{\tau}\mathbf{x} = 0 \tag{48}$$

where τ is the time constant of the system. $T = 5\tau$ is the time needed for the state to reach the 67% of its initial condition, in this case defined by $\mathbf{v} = 1$. In conclusion, it has been shown how force fields can be treated in Chrono::Engine and how increasing the number of fans permits to obtain better performances in stopping the particles, acting in all the three principal directions. A "rough" expression of the force has been considered in this example, but it wants to show the potential of Chrono::Engine in treating these kind of problems. This can be the base simulation to develop a more complex one, adding optical properties that can be managed by electromagnetic force fields and involving a greater number of particles with interactions between them.

D. Magnetic Levitation Model

It is possible to imagine the fan as the surface of the electromagnet, with a sphere suspended in the air very close to it due to an electromagnetic force. For the purpose of the present simulation, just consider the force acted on the sphere simply depending on the position of the sphere with respect to the electromagnet x_s and on the current applied I_c. Even if it is know that the dynamics of the system depends on other parameters, all those are considered known and constant in time. Therefore, the electrical part alone was neglected for the simulation.

$$V_c(t) = L_c\dot{I}_c(t) + (R_c + R_s)I_c(t) \tag{49}$$

The differential equation which govern the motion of the sphere is the following

$$M_s\ddot{x}_s = -F_c(t) + F_g(t) \tag{50}$$

where

$$F_c(t) = \frac{K_m I_c^2(t)}{2x_s^2(t)} \tag{51}$$

$$F_g(t) = M_s g \tag{52}$$

These lead to

$$\ddot{x}_s = -\frac{K_m I_c^2(t)}{2M_s x_s^2(t)} + g \tag{53}$$

In equation (53), K_m is the magnetic force constant for the electromagnet/sphere pair and M_s is the mass of the sphere. Therefore, the only part that needs to be implemented in Chrono::Engine if the electromagnetic force $F_c(t)$. Since the aim of the present simulation is to show that given a current $I_c(t)$, the result of the simulation is a stable oscillation near an equilibrium position, a control has not been introduced yet, and the current has been considered constant. Therefore $I_c(t) = I_c$. Defining an error e as the difference between the actual position of the particle and the desired one, and the same for their derivatives as follows

$$e(t) = x_s(t) - x_d \tag{54}$$

$$\dot{e}(t) = \dot{x}_s(t) - \dot{x}_d \tag{55}$$

where x_d and $\dot{x}_d$ are the desired position and velocities of the particle. The control is introduced in such a way that the current is proportional to the error and to its derivative

$$I(t) = k_p e(t) + k_d \dot{e}(t) \tag{56}$$

It is possible to change k_p and k_d parameters in order to have different behaviors of the transient of the particle, in order to reduce oscillations or the settling time. One thing that can be improved of the previous model, is that there is a discontinuity on the force at the beginning because of the immediate distance between the particle and the magnet (0.040 m). This can be avoided imposing a ramp as starting behavior of the force. It is also possible to impose some constraints on the value of the current if someone wants to stay under a certain limit. In the case of 100 spheres controlled by different fans, with independent control low, the result is shown if Fig. 21. It can be seen that with the same particle and control parameters, as expected, the same final position is reached by every particle having independent control law one with respect to the other even if the initial conditions are different.

E. Inverse determination of electric and magnetic fields for cloud re-shaping

A molecular dynamics simulation effort was also conducted. The problem is treated as a coupled set of semi-discrete differential equations for each grain. Given the position and velocity of each particle at one time step, the algorithm estimates these values at the next time step. To compute the next position of each particle requires the evaluation of the right hand side of its corresponding differential equation. Since each of these calculations is independent, there is a potential speedup if the program can take advantage of parallel computing. A Gaussian random process generator generates an initial distribution of grains. The cloud is placed in an orbit identified by the six classical orbital elements. The cloud is subject to gravitational

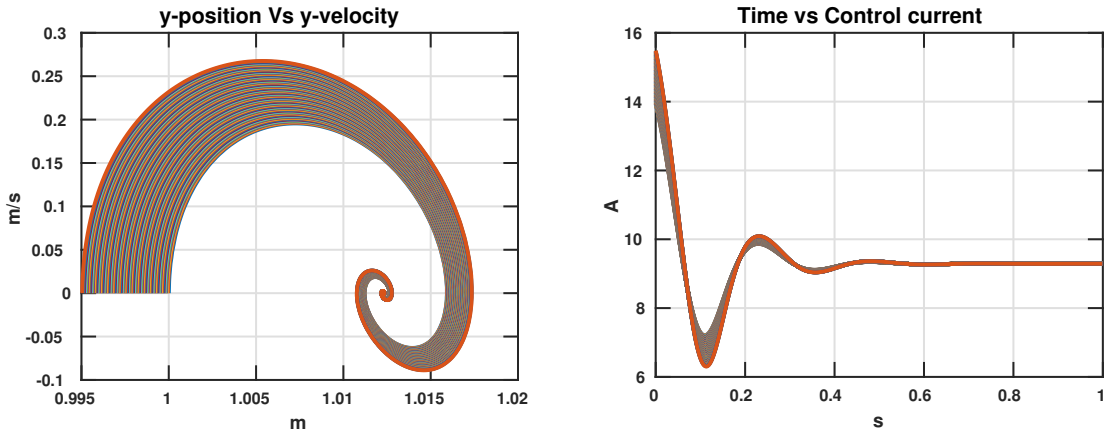

Figure 21. (left) y-position Vs y-velocity in the case of 100 spheres. (right) Time Vs current I(t) in the case of 100 spheres

harmonics from the Earth (JGM3 Earth gravity model, with 20 harmonic components). Currently, we are adding third-body disturbances from the Sun and the Moon, solar radiation pressure, and atmospheric drag. Figure 22 shows a system with 1000 spherical grains in the form of a paraboloid surface, with all the grain normals aligned towards the focus of the paraboloid. Since there is no control, the cloud evaporates within a fraction of the orbital period. The simulation results shown in Figure 22 were obtained by commanding the grains to conform to a prescribed optical surface. The cloud is first shaped into a disk, then into a paraboloid of specified focal length and diameter. The numerical results indicate that the force required to shape 1 meter diameter disk into parabola is of the order of 10-8 N. Assuming a grain shape which is asymmetric to incoming light, the torque required to align 1 micron grain is of the order of 10-15 Nm.

We can derive an control law to track a desired surface as follows. Define the tracking error

$$e_Z = q(x, y) - q_d(x, y) \tag{57}$$

where $q_d(x, y)$ describes the desired surface, and $q(x, y)$ the current position of the grain with respect to the origin of the orbiting reference frame. By imposing an exponentially stable error dynamics in the form:

$$\ddot{e}_Z + 2\xi\omega\dot{e}_Z + \omega^2 e_Z = 0 \tag{58}$$

where ω is the natural frequency, and ξ the damping ratio, we can make sure the error e_Z is driven to zero. Therefore, using the equations of mo:on expressed in the moving frame (the orbiting reference frame - ORF), the control law with components in ORF becomes:

$$u = -f_{pert} + f_{gyro} + m\ddot{q}_{des} - K_d\dot{e}_Z - K_p e_Z \tag{59}$$

where f_{pert} is the resultant of perturbation forces on the grain (gravity, solar pressure, etc),f_{gyro} are the Coriolis and centrifugal forces acting on the grain, K_d is a derivative gain, and K_p is a proportional gain.

Once the control force to shape the cloud has been computed, the electric and magnetic field to produce that re-shaping can be computed as follows.

A grain, of mass m and charge q, moving with inertial velocity $\mathbf{v}$, and subject to an electric field $\mathbf{E}$ and to a magnetic field $\mathbf{B}$, is subject to a Lorentz force given by:

$$\mathbf{f_L} = \mathbf{q}(\mathbf{E} + \mathbf{v} \times \mathbf{B}) \tag{60}$$

In components in ORF, we obtain:

$$u = f_L = q(I_{33}E + v^{\times}B) = q\begin{pmatrix} I_{33} & v^{\times} \end{pmatrix} \begin{pmatrix} E \\ B \end{pmatrix} \tag{61}$$

where I_{33} is the 3×3 identity matrix, and the operator $(v)^{\times}$ denotes the skew-symmetric matric operator associated with the vector product. Using the matrix pseudo-inverse operation $(v)^{\dagger}$, we obtain:

$$\begin{pmatrix} E \\ B \end{pmatrix} = q\begin{pmatrix} I_{33} & v^{\times} \end{pmatrix}^{\dagger} u \tag{62}$$

Figures 23, and Figures 24 show the components of the electric and magnetic field, as a function of Julian date, involved in the trapping mechanism required to rigidly retarget the parabolic shaped cloud of 60 degrees about the x-axis (in cloud body frame).

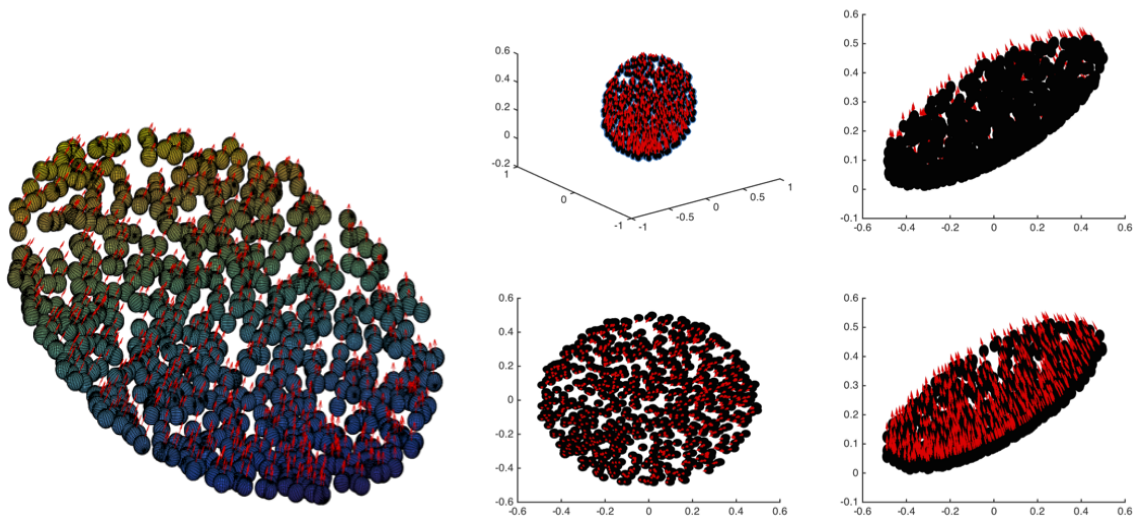

Figure 22. (left) N=1000 grains aligned to wavefront. (right) Projections.

VI. Conclusions

This paper has described the modeling and simulation of trapped granular media, within the context of the Granular Imager project. After describing the physics of trapped granular media in space, we discussed the methodologies used to stably confine and shape such a medium using electromagnetic fields. The numerical models have also been validated with results in the literature, obtaining excellent agreement. The results of the numerical tests indicate that it is possible, with structural arrangements of rings and plates at different levels of electrostatic potential, to stably confine one or more charged particles, when driven by voltages that can be modulated in time and space.

Near-term proof-of-concept space demonstrations of the Granular Imager might be possible within a decade, but laboratory-scale tests on Earth are possible much sooner. This concept is technically feasible given that it is drawn from real-world examples of dust/droplet systems like rainbows. Our solution would completely rewrite our approach to ultra-large space-based telescopes for potential military applications. All the foundations of the concept are solidly based on established physical laws. The challenge is extending what has been proven in small lenses in an Earth environment to a space environment under various forces and the means to predict and control those forces for a long time to get the full benefit of the concept. There is no guarantee that this breakthrough innovative system will meet the configuration or design of a large aperture system at various parts of the electromagnetic spectrum, but even if a few of those areas are or can be identified, the benefit for NASA will be immense.

Acknowledgement This research was carried out at the Jet Propulsion Laboratory, California Institute of Technology, under a contract with the National Aeronautic and Space Administration under the NASA Innovative Advanced Concepts Program. The authors are grateful to Prof. Alessandro Tasora of the University of Parma, Italy, and Professor Francesco Braghin or the Politecnico di Milano, Italy, for clarifying some technical aspects related to the Chrono simulator.

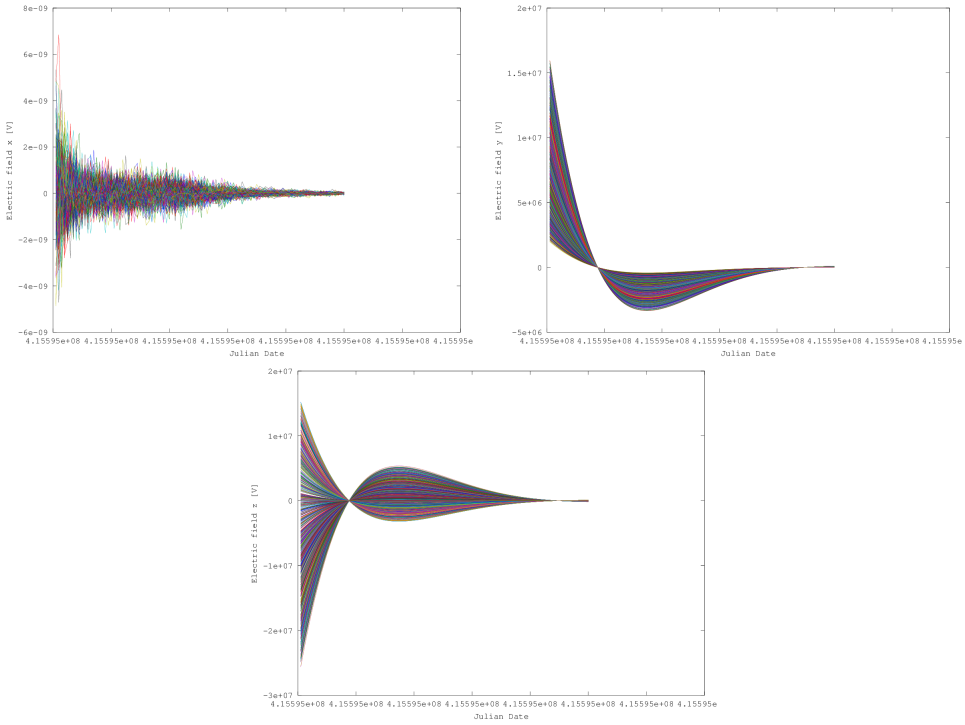

Figure 23. X-, Y-, and Z-component of Electric field needed to rigidly retarget the parabolic shaped cloud of 60 degrees about the x-axis (in cloud body frame).

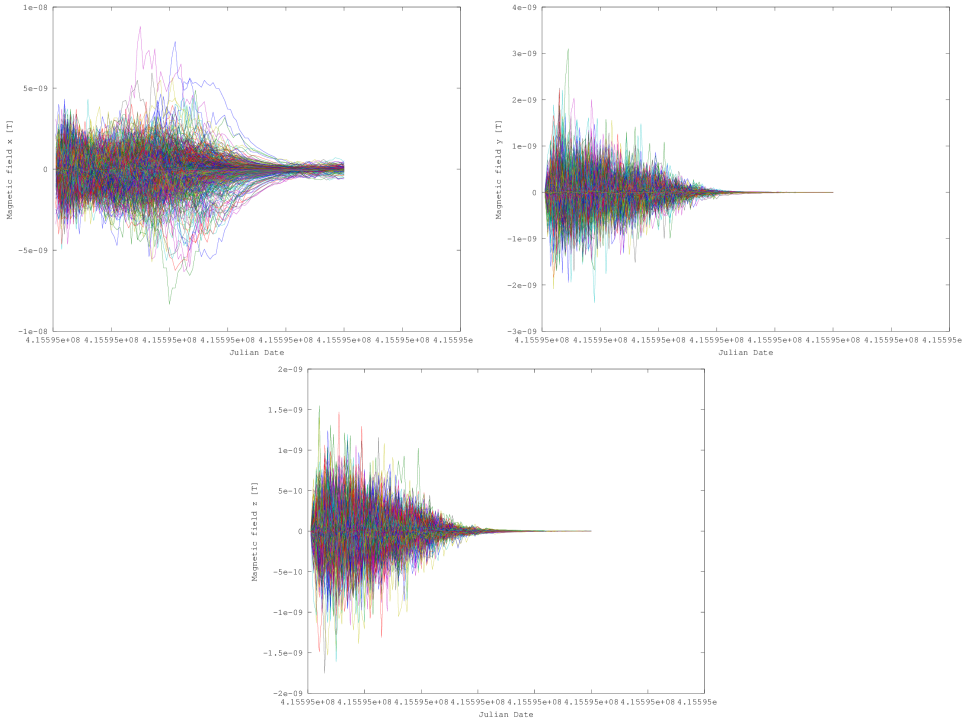

Figure 24. X-, Y-, and Z-component of Magnetic field needed to rigidly retarget the parabolic shaped cloud of 60 degrees about the x-axis (in cloud body frame).

References

[1]Ashkin, A.: Acceleration and trapping of particles by radiation pressure, Phys. Rev. Lett. 24. 156-159, 1970.

[2]Davis, E.J., and Schweiger, G.: The Airborne Microparticle, Springer, 2012.

[3]https://projectchrono.org

[4]Eringen ,C.: Microcontinuum Field Theories, Springer Verlag, 1999.

[5]Fuchs, N.A.: The Mechanics of Aerosols, Dover Publications, 1989.

[6]Gosh, P.K.: Ion Traps, Clarendon Press, Oxford 1995, p.18

[7]Greengard, L.: The numerical solution of the N-body Problem, Computers in Physics, March-April 1990, pp. 142-152.

[8]Grzegorczyk, T., Kemp, B. A., Kong, J.A.: Trapping and binding of an arbitrary number of cylindrical particles in an in-plane electromagnetic field, J. Opt. Soc. Am. A, 23(9) Sept. 2006.

[9]Grzegorczyk, T., Kemp, B. A., Kong, J.A.: Passive guiding and sorting of small particles with optical binding forces, Opt. Lett., 31(22), Nov. 2006.

[10]Labeyrie, A.: Standing Wave and Pellicle: A Possible Approach to Very Large Space Telescopes, Astronomy and Astrophysics, 77, L1-L2, 1979.

[11]Mogilner, A., Edelstein-Keshet, L.: A Non-local Model for a Cloud, Journal of Mathematical Biology, 1999, no. 38, pp. 534-570.

[12]Molmud, P., Expansion of a Rarefield Gas Cloud into a Vacuum, The Physics of fluids 3, 362-366 (1960).

[13]Palmer, A.J.: Radiation-induced Orientation of Atmospheric Aerosols, J. OP. Soc. America A, vol. 8, no. 2, February 1991.

[14]Pfalzner, S, and Gibbon, P.: Many-Body Tree Methods in Physics, Cambridge University Press, 1996.

[15]Quadrelli, M., Basinger, S., Swartzlander, G.: Dynamics and Control of a Disordered System In Space, AIAA SPACE 2013 Conference, San Diego, Ca, Sept. 2013.

[16]Quadrelli, B.M., Basinger S., Palacios, D., Arumugam, D.: Dynamics and Control of Granular Imaging Systems, presented at AIAA SPACE 2015 Conference, Pasadena, CA, Sept. 2015.

[17]Quadrelli, B.M., Basinger S., Palacios, D., Arumugam, D., Swartzlander, G.: Orbiting Rainbows, presented at SPIE Photonics, San Diego, CA, August 2015.

[18]Quadrelli, M., Mazhar, H., Negrut, D.: Modeling and Simulation of AnchoringProcesses for Small Body Exploration, AIAA SPACE 2012 paper. AIAA2012-5310.

[19]Reif, J.H., and Wang, H., Social Potential Fields: A Distributed Behavioral Control for Autonomous Robots, Robotics and Autonomous Systems 27 (1999) 171-194.

[20]Siljak, D.D.: Decentralized Control of Complex Systems, Academic Press, 1990.

[21]Schuster, D.L: Dynamic Response of Dielectric Lenses Influenced By Radiation Pressure, M.S. Thesis , R.I.T., 2014.

[22]Simpson, S., Hanna, S., Peterson, T., and Swartzlander, G., "Optical lift from dielectric semicylinders," Opt. Lett. 37, 4038-4040 (2012).

[23]Verma, N.K.: Multiparticle Trajectory Simulation for Ion Trap Mass Spectrometers, M.A. Thesis, Indian Institute of Technology, July 2008, p.41

[24]S. J. Zaroodny, An Elementary Review Of The Mathieu-Hill Equation Of Real Variable Based On Numerical Solutions, Memorandum Report No. 878, APRIL 1955, pp.6-7